Simulations of Dipole Surface Current Distributions and Radiation Patterns

Master's Thesis by

Patrick B. Sørensen & Jes L. Thomsen

Department of Materials and Production
Aalborg University

SIMULATIONS OF DIPOLE SURFACE CURRENT DISTRIBUTIONS AND RADIATION PATTERNS

Master's thesis by

Patrick B. Sørensen & Jes L. Thomsen
Aalborg University, Skjernvej 4A, DK-9220 Aalborg Øst

Supervised by

Associate Professor Thomas Søndergaard
Aalborg University, Skjernvej 4A, DK-9220 Aalborg Øst

Abstract

This thesis employ the method of moments, a numerical integral equation method, to model the induced surface currents on metallic antennas located on a semiconductor substrate. The purpose is to gain insight into modelling photoconductive antennas for THz generation. The electric field integral equation and the dyadic Green's tensor for a planar interface between isotropic media is obtained. Using the method of moments, the electric surface currents induced on a perfect electric conductor by an incident field is acquired, which allows for the calculation of scattered fields. A MATLAB script, which calculates the induced current on an arbitrary three-dimensional perfect electric conductor, and the scattered electric field have been produced, as well as the far-field scattered radiation pattern for antenna structures located on a semiconductor substrate. A possible short coming of the method of moments was identified, namely that a variation in the cross sectional surface current was present when the excitation source was an incident plane-wave. A possible solution to this was presented as a voltage feed excitation method. Using this method, the radiation patterns for antenna arrays with different inter antenna distances placed on a substrate was presented, and a possible optimal inter antenna distance was proposed.

Submitted on the 1st of June 2018
Number of pages: 80
Number of appendices: 4

Preface

This thesis has been composed during the author's Master's degree in physics from the Department of Materials and Production at Aalborg University.
The report is written in ShareLaTeX, which is an online cooperative version of LaTeX. Figures without citation were made by the authors using either MATLAB, Inkscape or TikZ. The STL files used are created using CAD in Fusion360, the meshes are auto-generated by Fusion360. Figure and table references are formatted by chapter and number of the specific figure or table in the chapter (example: Figure 3.2; Chapter 3 figure number 2). The equation references can be found to the right of the equation and are formatted by chapter and the number in the chapter (example: (2.3); Chapter 2 equation number 3). Citations are made using the IEEE referencing style, i.e. sources are referenced by number and sorted in the order they appear in the thesis (example: [1]).
Lastly, we would like to thank our supervisor, Thomas Søndergaard, for the help and knowledge provided during the production of this thesis.

Patrick B. Sørensen
Jes L. Thomsen

Patrick B. Sørensen

Jes L. Thomsen

Contents

List of Figures

List of Tables

Nomenclature

Abbreviations

CAD	Computer aided software
EFIE	Electric field integral equation
MoM	Method of Moments
PEC	Perfect electric conductor
RWG	Rao-Wilton-Glisson
THz	Terahertz

Notations

$\boldsymbol{\varrho}$	RWG basis function vector
δ	Dirac delta function
$\hat{\mathbf{a}}$	Unit vector
$\langle . , . \rangle$	Inner product
$\mathcal{L}$	Linear operator
$\mathcal{O}$	Big O notation
$\bar{\bar{A}}$	Matrix
$\overleftrightarrow{\mathbf{A}}$	Tensor
$\mathbf{A}, \mathbf{a}$	Vector
$\mathbf{ab}$	Outer product between vectors $\mathbf{a}$ and $\mathbf{b}$.
A, a	Scalar quantity

Symbols/Constants

μ Permeability of a specific medium

ε Permittivity of a specific medium

c Speed of light in vacuum

CHAPTER 1

Introduction

The purpose of this thesis is to model metallic antennas which will pertain to the modeling of antennas for *terahertz* (THz) generation. The main focus is on utilizing the *method of moments* (MoM), an integral equation method, to model the antenna radiation. Since THz wavelengths are relatively long compared to the optical domain it is possible to approximate the metallic antennas as *perfect electrical conductors* (PEC).

THz radiation lies between the microwave and infrared frequencies, and for many years the part of the THz regime which roughly spans from 100 GHz to 10 THz has been referred to as the THz-gap due to the lack of powerful sources and detectors. In the last few decades, the advances in the semiconductor and nanotechnology have made it possible to access this unused regime, and multiple applications that utilizes these frequencies have since been proposed by researchers from various scientific areas. [2]

THz waves have many potential usages. The wavelength is short enough to obtain sub-millimeter level spatial resolution, and in medical imaging, the use of THz waves for detecting skin and other surface cancers has been developed, as well as an intraoperative tool during breast cancer surgery to confirm in real-time the removal of cancer tissue [3]. THz waves have low photon energies and cannot photoionize biological tissues as compared to X-rays, and are therefore considered safe. Many molecules show strong absorption and dispersion at THz frequencies, which can be used as as a spectroscopic fingerprints. And since THz waves are transparent to most dry dielectric materials, e.g. cloth, paper and plastic, this opens up for the potential use of THz in detection of concealed or covered objects [4]. This includes the standoff detection of explosives, and noxious gasses. In the photovoltaic industry, THz radiation can be use in detection and imaging of cracks

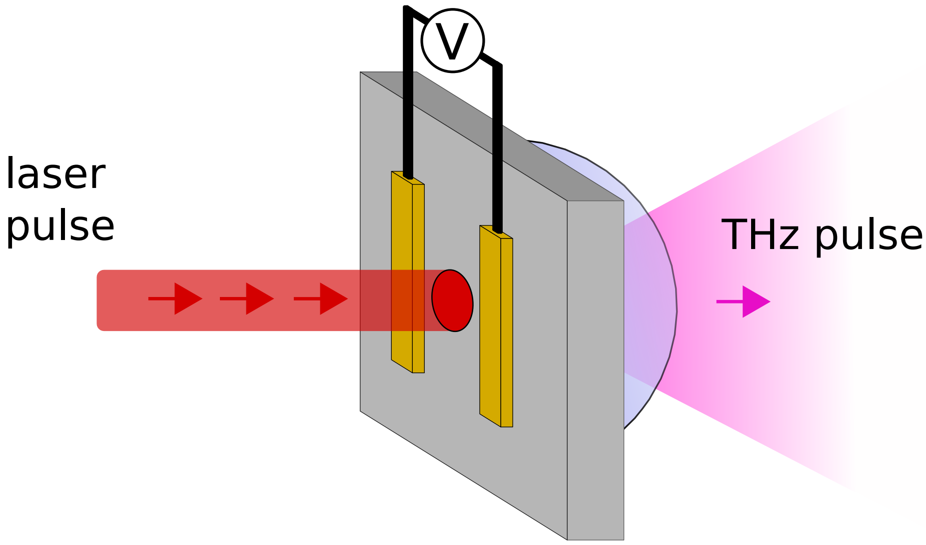

FIGURE 1.1 – Illustration of a photoconductive antenna: two metallic antennas are placed on a photoconductive substrate with a bias voltage applied. A laser pulse illuminates the gap between the two antenna, which excites electrons and holes in the substrate. Due to the bias voltage, THz generating currents are formed.

and defects buried in silicon, as well as inspection and quality control of coatings [3]. It is safe to say the number of areas in which THz can be used are vast.

The generation of THz radiation and detection can be achieved by the use of photoconductive antennas, or via optical rectification. A typical photoconductive antenna is shown in Figure 1.1. Two electrodes (antennas) are located on a photoconductive substrate, such as silicon or gallium arsenide, with a bias voltage applied to the antennas. When the gap between the antennas are illuminated by a laser beam with higher energy that the bandgap energy of the substrate, electrons and holes are generated and will due to the voltage bias form currents. It is these time varying currents that will generate the THz radiation. Two important parameters are the length of the metallic antennas and the distance between.

In Chapter 2, the theoretical preliminaries needed in order to analyze electromagnetic scattering of a perfect electric conductor are discussed. From Maxwell's equations the inhomogeneous Helmholtz equation is derived, as well as the *electric field integral equation* (EFIE) for a perfect electric conductor. The derivation of the dyadic Green's tensor is made and rewritten into cylindrical coordinates before extending the dyadic Green's tensor to accommodate for a planer interface between two isotropic media. The chapter concludes with an introduction to the method of moments, an numerical method for solving linear operator equations, and an example of how the method can be applied to an arbitrary three-dimensional surface.

Chapter 3 discussed the script that implements the method of moments in MATLAB. The chapter contains a walkthrough the scripts structure, covering the overarching operations from import of antenna structure to solving the MoM, to computing and visualizing the current and finally different ways of computing the radiated electric field. In addition some thoughts behind the implementation are presented alongside limitations regarding input and options.

The results acquired from the implemented MATLAB script are presented in Chapter 4. The surface currents induced by different excitation sources are presented, as well as the far-field radiation patterns for half-wave dipoles. The use of a voltage feed as an excitation source for different dipoles, and the far-field radiation patterns for dipoles located on a silicon substrate are examined.

Chapter 5 contains discussion of the results, followed by conclusions presented in Chapter 6.

CHAPTER 2

THEORETICAL PRELIMINARIES

THIS chapter establishes the theoretical foundation required to analyze the radiation scattered of a perfect electric conductor near a planar interface. The inhomogeneous Helmholtz equation is derived from Maxwell's equations, followed by derivation of the electric field integral equation for scattering of a perfect conducting surface. The dyadic Green's tensor for the electric field is derived, and rewritten into cylindrical coordinates. An expression for the Green's tensor for a two-layered planar interface is obtained, followed by a presentation of the method of moments and it's application to an arbitrary three-dimensional perfect electric conductor.

2.1 MAXWELL'S EQUATIONS

This section will summarize Maxwell's equations, and the electromagnetic boundary conditions needed in order to analyze the radiation produced by electric currents induced on a perfect electric conductor. The inhomogeneous Helmholtz equation and the electric field integral equation are derived in the following subsections.

The differential form of Maxwell's equations relates electric and magnetic field vectors to current densities and charge densities at any point in space-time where the fields are continuously differentiable. For a linear isotropic medium, Maxwell's equations in the frequency-domain are given by

$$\nabla \times \mathbf{E} = -i\omega\mu\mathbf{H}\,, \tag{2.1}$$

$$\nabla \times \mathbf{H} = i\omega\varepsilon\mathbf{E} + \mathbf{J}\,, \tag{2.2}$$

$$\nabla \cdot \mathbf{D} = \rho\,, \tag{2.3}$$

$$\nabla \cdot \mathbf{B} = 0\,, \tag{2.4}$$

where $\mathbf{E}$ is electric field intensity, $\mathbf{H}$ is magnetic field intensity, $\mathbf{D} = \varepsilon\mathbf{E}$ is electric flux density, $\mathbf{B} = \mu\mathbf{H}$ is magnetic flux density, $\mathbf{J}$ is electric current density, ρ is electric charge density, ε is electric permittivity, and μ is magnetic permeability. [5] Notice that we have assumed a $e^{-i\omega t}$ time dependency, which will be suppressed throughout the thesis.

At interfaces between media, the vector quantities in Maxwell's equations may not be differentiable, and we instead require the fields to satisfy some boundary conditions, which relates the tangential and normal components of the vector fields. For the interface between two arbitrary media, the boundary conditions can in general be expressed as

$$\hat{\mathbf{n}} \times (\mathbf{E}_1 - \mathbf{E}_2) = 0\,, \tag{2.5}$$

$$\hat{\mathbf{n}} \times (\mathbf{H}_1 - \mathbf{H}_2) = \mathbf{J}_s\,, \tag{2.6}$$

$$\hat{\mathbf{n}} \cdot (\mathbf{D}_1 - \mathbf{D}_2) = \rho_s\,, \tag{2.7}$$

$$\hat{\mathbf{n}} \cdot (\mathbf{B}_1 - \mathbf{B}_2) = 0\,, \tag{2.8}$$

where $\hat{\mathbf{n}}$ is the unit normal vector on the interface with direction from medium 1 to medium 2, $\mathbf{J}_s$ is surface current density, and ρ_s is the surface change density. [5] If one of the two media is a *perfect electric conductor* (PEC), e.g. medium 2, the boundary conditions can be reduced to

$$\hat{\mathbf{n}} \times \mathbf{E}_1 = 0\,, \tag{2.9}$$

$$\hat{\mathbf{n}} \times \mathbf{H}_1 = \mathbf{J}_s\,, \tag{2.10}$$

$$\hat{\mathbf{n}} \cdot \mathbf{D}_1 = \rho_s\,, \tag{2.11}$$

$$\hat{\mathbf{n}} \cdot \mathbf{B}_1 = 0\,, \tag{2.12}$$

since $\mathbf{E}_2 = 0$. This means that the electric field $\mathbf{E}_1$ on the surface of a PEC only has a normal component. The same statement holds true for the electric flux density $\mathbf{D}_1$.

2.1.1 *Radiated Electric Fields*

In the following, the inhomogeneous Helmholtz equation and an integral equation for the electric field will be derived. We start by taking the curl of Eq. (2.1) to obtain

$$\nabla \times \nabla \times \mathbf{E} = -i\omega\mu\nabla \times \mathbf{H}\,, \tag{2.13}$$

and next apply the vector identity

$$\nabla \times \nabla \times \mathbf{E} = \nabla\left(\nabla \cdot \mathbf{E}\right) - \nabla^2\mathbf{E}\,, \tag{2.14}$$

in order to restate Eq. (2.13) as

$$\nabla\left(\nabla \cdot \mathbf{E}\right) - \nabla^2\mathbf{E} = -i\omega\mu\nabla \times \mathbf{H}\,. \tag{2.15}$$

By substituting Eq. (2.2) into Eq. (2.15) we get

$$\nabla\left(\nabla \cdot \mathbf{E}\right) - \nabla^2\mathbf{E} = -i\omega\mu\mathbf{J} + k^2\mathbf{E}\,, \tag{2.16}$$

where $k^2 = \omega^2\mu\varepsilon$. Taking the divergence of Eq. (2.2) yields

$$\begin{aligned}\nabla \cdot \nabla \times \mathbf{H} &= \nabla \cdot \mathbf{J} + i\omega\nabla \cdot \mathbf{D} \\ &= \nabla \cdot \mathbf{J} + i\omega\rho\,,\end{aligned} \tag{2.17}$$

and since the divergence of a curl equals zero, it follows that

$$\nabla \cdot \mathbf{J} = -i\omega\rho\,. \tag{2.18}$$

Now consider the parenthesis on the left-hand side of Eq. (2.16). This can be rewritten using Eq. (2.3) as

$$\nabla \cdot \mathbf{E} = \frac{1}{\varepsilon}\nabla \cdot \mathbf{D} = \frac{\rho}{\varepsilon}\,. \tag{2.19}$$

By utilizing Eqs. (2.18) and (2.19), the parenthesis in Eq. (2.16) can be expressed as

$$\nabla \cdot \mathbf{E} = \frac{i}{\omega\varepsilon}\nabla \cdot \mathbf{J}\,. \tag{2.20}$$

By substituting Eq. (2.20) into (2.16) and rearranging, we arrive at the inhomogeneous Helmholtz equation:

$$\nabla^2\mathbf{E} + k^2\mathbf{E} = i\omega\mu\mathbf{J} + \frac{i}{\omega\varepsilon}\nabla\left(\nabla \cdot \mathbf{J}\right)\,. \tag{2.21}$$

Equation (2.21) can be solved by means of Green's functions. The concept of Green's functions is further explained in Section 2.2. By using this method, it is possible to show that the solution to Eq. (2.21) is given by

$$\mathbf{E}(\mathbf{r}) = -i\omega\mu\int \overleftrightarrow{\mathbf{G}}(\mathbf{r},\mathbf{r}') \cdot \mathbf{J}(\mathbf{r}')\,d\mathbf{r}'\,, \tag{2.22}$$

where

$$\overleftrightarrow{\mathbf{G}}(\mathbf{r},\mathbf{r}') = \left(\overleftrightarrow{\mathbf{I}} + \frac{1}{k^2}\nabla\nabla\right) g(\mathbf{r},\mathbf{r}'), \quad g(\mathbf{r},\mathbf{r}') = \frac{e^{ik|\mathbf{r}-\mathbf{r}'|}}{4\pi|\mathbf{r}-\mathbf{r}'|}\,. \tag{2.23}$$

The expression given by Eq. (2.23) is known as the dyadic Green's tensor. A derivation is included in Section 2.2.

2.1.2 *Scattered Electric Fields*

The scattering of electromagnetic waves of a PEC can be viewed as radiation emitted by the PEC itself, where the radiating currents located on the scatter are themselves generated by external fields. If the induced current $\mathbf{J}$ is known, the scattered field can be calculated from by

$$\mathbf{E}_s(\mathbf{r}) = -i\omega\mu \iint_S \overleftrightarrow{\mathbf{G}}(\mathbf{r},\mathbf{r}')\cdot\mathbf{J}(\mathbf{r}')\,d\mathbf{r}'\,. \tag{2.24}$$

However, the current $\mathbf{J}$ may not be known initially, or might not even have an analytic solution. In those situations, $\mathbf{J}$ must therefore be numerically solved for. Consider the boundary conditions of the electric field at the surface of the PEC:

$$\hat{\mathbf{n}}(\mathbf{r})\times\mathbf{E}_s(\mathbf{r}) = -\hat{\mathbf{n}}(\mathbf{r})\times\mathbf{E}_i(\mathbf{r})\,, \tag{2.25}$$

where $\hat{\mathbf{n}}(\mathbf{r})$ is the surface normal.
By combining Eqs. (2.24) and (2.25), we can now formulate the *electric field integral equation* (EFIE) for a perfect conducting surface,

$$-\frac{i}{\omega\mu}\hat{\mathbf{n}}(\mathbf{r})\times\mathbf{E}_i(\mathbf{r}) = \hat{\mathbf{n}}\times\iint_S \overleftrightarrow{\mathbf{G}}(\mathbf{r},\mathbf{r}')\cdot\mathbf{J}(\mathbf{r}')\,d\mathbf{r}'\,. \tag{2.26}$$

The EFIE is also sometimes expressed in terms of the magnetic vector potential $\mathbf{A}(\mathbf{r})$:

$$-\frac{i}{\omega\mu}\hat{\mathbf{n}}(\mathbf{r})\times\mathbf{E}_i(\mathbf{r}) = \hat{\mathbf{n}}\times\left[1+\frac{1}{k^2}\nabla\nabla\cdot\right]\mathbf{A}(\mathbf{r})\,. \tag{2.27}$$

For an arbitrarily shaped PEC, the EFIE relates the tangential component of the incident electric field to the tangential component of the scattered field at the surface of the PEC. If the incident field $\mathbf{E}_i$ is known, the unknown current $\mathbf{J}$ can be solved numerically by the method of moments described in Section 2.4. Once the current has been solved for, Eq. (2.24) can be used to obtain the scattered electric field.

2.2 GREEN'S FUNCTION INTEGRAL METHOD

The section will present the Green's function integral method. The following subsections will contain derivations of the 3D free-space Green's function for the electric field, and the dyadic Green's tensor.

Green's functions are mathematical tools that can be used to find solutions to ordinary differential equations with initial value conditions, or even more complicated equations such as inhomogeneous partial differential equations with boundary conditions. In electrodynamics, Green's functions are widely used to solve differential equations which are difficult or impossible to find exact solutions to, but also in other disciplines are the Green's functions often used, e.g. in quantum field theory they are used as propagators .
Consider a inhomogeneous differential equation of the form

$$\mathcal{L}u(\mathbf{r}) = f(\mathbf{r}) \,, \tag{2.28}$$

where $\mathcal{L}$ is a linear differential operator, $u(\mathbf{r})$ is a unknown function.
The Green's function $g(\mathbf{r}, \mathbf{r}')$ is defined as the inverse of the operator $\mathcal{L}$, and satisfy the equation

$$\mathcal{L}g(\mathbf{r}, \mathbf{r}') = \delta(\mathbf{r} - \mathbf{r}') \,, \tag{2.29}$$

where $\delta(\mathbf{r} - \mathbf{r}')$ is the Dirac delta function.

$$\int \mathcal{L}g(\mathbf{r}, \mathbf{r}')f(\mathbf{r}')\, d\mathbf{r}' = \int \delta(\mathbf{r} - \mathbf{r}')f(\mathbf{r}')\, d\mathbf{r}' \,. \tag{2.30}$$

Since $\mathcal{L}$ is an linear operator that only operates on $\mathbf{r}'$, Eq. (2.30) can be written as

$$\mathcal{L}\left(\int g(\mathbf{r}, \mathbf{r}')f(\mathbf{r})\, d\mathbf{r}'\right) = \int \delta(\mathbf{r} - \mathbf{r}')f(\mathbf{r}')\, d\mathbf{r}' = f(\mathbf{r}) \,, \tag{2.31}$$

where the last equality follows from the properties of the Dirac delta function.
From Eq. (2.31) it can be seen that a solution to Eq. (2.28) is given by

$$u(\mathbf{r}) = \int g(\mathbf{r}, \mathbf{r}')f(\mathbf{r}')\, d\mathbf{r}' \,. \tag{2.32}$$

The method used for solving for $u(\mathbf{r})$ in Eq. (2.28) is essentially the method of moments, described in Section 2.4, which can be utilized when $\mathcal{L}$ is an linear operator.

2.2.1 *Free-Space Green's Function*

In order to derive the free-space Green's function, we make use of Helmholtz's theorem, which states, that any continuous vector field $\mathbf{F}$ can be decomposed into the sum of a gradient and a curl term, i.e.

$$\mathbf{F} = -\nabla\Phi + \nabla \times \mathbf{A} \,, \tag{2.33}$$

where Φ is the scalar potential, and $\mathbf{A}$ is the vector potential. [6]

If no free charges are present in the medium, Eq. (2.3) implies that **H** can be written as

$$\mathbf{H} = \frac{1}{\mu}\nabla \times \mathbf{A}\,. \tag{2.34}$$

Combining Eq. (2.34) and Eq. (2.1) allows us to write

$$\nabla \times (\mathbf{E} + i\omega\mathbf{A}) = 0\,, \tag{2.35}$$

and by utilizing Helmholtz's theorem again, it follows that

$$\mathbf{E} + i\omega\mathbf{A} = -\nabla\Phi\,. \tag{2.36}$$

By taking the curl on both sides of Eq. (2.34), and applying the vector identity given by (2.14), yields

$$\mu\nabla \times \mathbf{H} = \nabla \times \nabla \times \mathbf{A} = \nabla\left(\nabla \cdot \mathbf{A}\right) - \nabla^2\mathbf{A} \tag{2.37}$$

When substituting Eq. (2.2) into (2.37), we find that

$$\nabla\left(\nabla \cdot \mathbf{A}\right) - \nabla^2\mathbf{A} = i\omega\mu\varepsilon\mathbf{E} + \mu\mathbf{J}\,, \tag{2.38}$$

and by using Eq. (2.36), Eq. (2.38) can be stated as

$$\nabla\left(\nabla \cdot \mathbf{A}\right) - \nabla^2\mathbf{A} = \mu\mathbf{J} - i\omega\mu\varepsilon\nabla\Phi + \omega^2\mu\varepsilon\mathbf{A}\,, \tag{2.39}$$

or rewritten as

$$\nabla^2\mathbf{A} + k^2\mathbf{A} = i\omega\mu\varepsilon\nabla\Phi + \nabla\left(\nabla \cdot \mathbf{A}\right) - \mu\mathbf{J}\,, \tag{2.40}$$

where $k^2 = \omega^2\mu\varepsilon$.
From Helmholtz's theorem, we are free to choose the divergence of **A**, so we conveniently choose

$$\nabla \cdot \mathbf{A} = -i\omega\mu\varepsilon\Phi\,. \tag{2.41}$$

Substituting Eq. (2.41) into (2.40) yields the vector Helmholtz equation,

$$\nabla^2\mathbf{A} + k^2\mathbf{A} = -\mu\mathbf{J}\,, \tag{2.42}$$

which must hold for all components of **A**. The Green's function for each component of Eq. (2.42) must satisfy the scalar inhomogeneous differential equation given by

$$\nabla^2 g(\mathbf{r},\mathbf{r}') + k^2 g(\mathbf{r},\mathbf{r}') = -\delta(\mathbf{r} - \mathbf{r}')\,. \tag{2.43}$$

With Eq. (2.43), we are essentially considering a point source and an observation point located at $\mathbf{r}'$ and $\mathbf{r}$, respectively.

Since the solution to Eq. (2.43) is for a point source, it must retain spherical symmetry and it is therefore adequate to only consider the radial term in the Laplace operator. The first term on the left-hand side of Eq. (2.43) can be written as

$$\begin{aligned}\nabla^2 g(\mathbf{r},\mathbf{r}') &= \frac{1}{r^2}\frac{\partial}{\partial r}\left(r^2\frac{\partial}{\partial r}g(\mathbf{r},\mathbf{r}')\right) \\ &= \frac{\partial^2}{\partial r^2}g(\mathbf{r},\mathbf{r}') + \frac{2}{r}\frac{\partial}{\partial r}g(\mathbf{r},\mathbf{r}') \\ &= \frac{1}{r}\frac{\partial^2}{\partial r^2}rg(\mathbf{r},\mathbf{r}')\,,\end{aligned} \tag{2.44}$$

where $r = |\mathbf{r}-\mathbf{r}'|$. By using the last equality in Eq. (2.44), the homogeneous variant of Eq. (2.43) can be formulated as

$$\frac{\partial^2}{\partial r^2}rg(\mathbf{r},\mathbf{r}') + k^2 rg(\mathbf{r},\mathbf{r}') = 0\,. \tag{2.45}$$

Since we have adopted the time dependency $e^{-i\omega t}$, the only physical meaningful solution to Eq. (2.45) for $r > 0$ is given by

$$g(\mathbf{r},\mathbf{r}') = C\frac{e^{ikr}}{r}\,, \tag{2.46}$$

where $r = |\mathbf{r}-\mathbf{r}'|$. In order to find a unique solution, we need to impose boundary conditions. We would require that $g(\mathbf{r},\mathbf{r}') \to 0$ as $r \to \infty$, which is already fulfilled by Eq. (2.46). In order to determine the constant C, we substitute Eq. (2.46) into Eq. (2.43) and integrate the expression over a sphere containing the origin,

$$C\iiint_V \left\{\nabla^2\frac{e^{ikr}}{r} + k^2\frac{e^{ikr}}{r}\right\} dV = -\iiint_V \delta(\mathbf{r}-\mathbf{r}')\,dV = -1\,, \tag{2.47}$$

where $dV = r^2\sin(\phi)d\theta d\phi$. The first integral on the left-hand side of Eq. (2.47) can be solved by using the Gauss' divergence theorem:

$$\begin{aligned}C\iiint_V \nabla^2\frac{e^{ikr}}{r}\,dV &= C\oiint_S \nabla\frac{e^{ikr}}{r}\cdot\hat{\mathbf{n}}\,dS \\ &= 4\pi C r^2\hat{\mathbf{r}}\cdot\nabla\frac{e^{ikr}}{r} \\ &= 4\pi C\,(ikr-1)\,e^{ikr}\,.\end{aligned} \tag{2.48}$$

The second integral has a solution given by

$$\begin{aligned} C \iiint_V k^2 \frac{e^{ikr}}{r}\, dV &= 4\pi k^2 C \int_0^r r e^{ikr}\, dr \\ &= 4\pi k^2 C \left(e^{ikr}\left[\frac{1}{k^2} + \frac{r}{ik}\right] - \frac{1}{k^2}\right) \\ &= 4\pi C \left(e^{ikr}\left[1 - ikr\right] - 1\right) . \end{aligned} \tag{2.49}$$

In the limit, where $r \to 0$, the approximation $e^{ikr} \simeq 1$ is considered valid and Eq. (2.49) goes towards zero. Equation (2.48), on the other hand, becomes $-4\pi C$. [7] The constant C in Eq. (2.47) can now be solved for, and the 3D free-space Green's function is thus given by

$$g(\mathbf{r}, \mathbf{r}') = \frac{e^{ik|\mathbf{r}-\mathbf{r}'|}}{4\pi|\mathbf{r}-\mathbf{r}'|} . \tag{2.50}$$

The solution to Eq. (2.42) can now be found using

$$\mathbf{A} = \mu \int_V \mathbf{J}(\mathbf{r}') g(\mathbf{r}, \mathbf{r}')\, d\mathbf{r}' . \tag{2.51}$$

When dealing with electric fields, the Green's function needs to relate all components of the source to all the fields components. This type of Green's function is referred to as the *dyadic Green's tensor*.

2.2.2 *Free-Space Dyadic Green's Tensor*

In order to find the dyadic Green's tensor, we consider the electric field wave equation, which can obtained by substituting Eq. (2.2) into Eq. (2.13):

$$\nabla \times \nabla \times \mathbf{E}(\mathbf{r}) - k^2 \mathbf{E}(\mathbf{r}) = -i\omega\mu \mathbf{J}(\mathbf{r}) . \tag{2.52}$$

By utilizing Eqs. (2.36) and (2.41), the electric field $\mathbf{E}$ can be found from

$$\begin{aligned} \mathbf{E} &= -i\omega \mathbf{A} - \frac{i}{\omega\mu\varepsilon} \nabla\nabla \cdot \mathbf{A} \\ &= -i\omega \left[1 + \frac{1}{k^2}\nabla\nabla\cdot\right] \mathbf{A} , \end{aligned} \tag{2.53}$$

where $\mathbf{A}$ is on the form of Eq. (2.51). If the electric field is produced by an infinitesimal current source $\mathbf{J}$, i.e. a point source, along the $\hat{\mathbf{x}}$-direction,

$$\mathbf{J}(\mathbf{r}) = -\frac{1}{i\omega\mu} \delta(\mathbf{r} - \mathbf{r}')\, \hat{\mathbf{x}} , \tag{2.54}$$

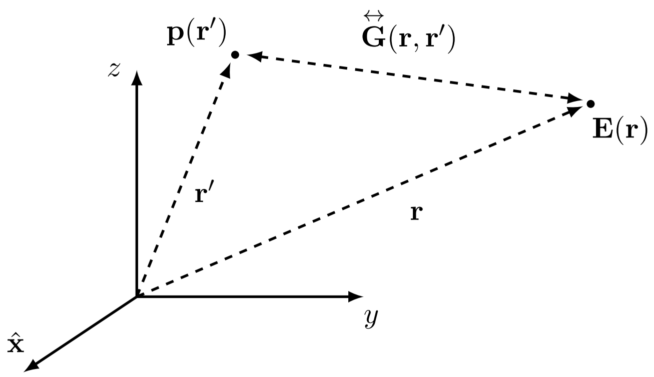

FIGURE 2.1 – The Green's tensor describes the electric field $\mathbf{E}$ at a field point $\mathbf{r}$ due to a point source $\mathbf{p}$ located at point $\mathbf{r}'$. The electric field at $\mathbf{r}$ depends on the orientation of $\mathbf{p}$ and the Green's function must therefore be a tensor in order to account for all possible orientations.

the electric field $\mathbf{E}$ can be calculated from

$$\mathbf{E} = -i\omega\mu \int_V \mathbf{G}_x(\mathbf{r},\mathbf{r}') \cdot \mathbf{J}(\mathbf{r}')\, d\mathbf{r}' \,, \tag{2.55}$$

where

$$\mathbf{G}_x(\mathbf{r},\mathbf{r}') = \left[1 + \frac{1}{k^2}\nabla\nabla\cdot\right] g(\mathbf{r},\mathbf{r}')\, \hat{\mathbf{x}} \,, \tag{2.56}$$

and $g(\mathbf{r},\mathbf{r}')$ is given by Eq. (2.50). If the $\mathbf{J}$ instead had been along the $\hat{\mathbf{y}}$- or $\hat{\mathbf{z}}$-direction, the electric field can be calculated by replacing $\hat{\mathbf{x}}$ with $\hat{\mathbf{y}}$ or $\hat{\mathbf{z}}$, respectively, to obtain

$$\mathbf{G}_y(\mathbf{r},\mathbf{r}') = \left[1 + \frac{1}{k^2}\nabla\nabla\cdot\right] g(\mathbf{r},\mathbf{r}')\, \hat{\mathbf{y}} \,, \tag{2.57}$$

or

$$\mathbf{G}_z(\mathbf{r},\mathbf{r}') = \left[1 + \frac{1}{k^2}\nabla\nabla\cdot\right] g(\mathbf{r},\mathbf{r}')\, \hat{\mathbf{z}} \,. \tag{2.58}$$

For an arbitrarily located point source $\mathbf{p} = \frac{1}{i\omega\mu}\delta(\mathbf{r}-\mathbf{r}')\,\hat{\mathbf{p}}$, the electric field can be calculated by combining Eqs. (2.56), (2.57), and (2.58) to form

$$\mathbf{E}(\mathbf{r}) = \overleftrightarrow{\mathbf{G}}(\mathbf{r},\mathbf{r}') \cdot \mathbf{p} \,, \tag{2.59}$$

where $\overleftrightarrow{\mathbf{G}}(\mathbf{r},\mathbf{r}') = \mathbf{G}_x(\mathbf{r},\mathbf{r}')\,\hat{\mathbf{x}} + \mathbf{G}_y(\mathbf{r},\mathbf{r}')\,\hat{\mathbf{y}} + \mathbf{G}_z(\mathbf{r},\mathbf{r}')\,\hat{\mathbf{z}}$.

By using the *unit dyadic* $\overleftrightarrow{\mathbf{I}} = \hat{\mathbf{x}}\hat{\mathbf{x}} + \hat{\mathbf{y}}\hat{\mathbf{y}} + \hat{\mathbf{z}}\hat{\mathbf{z}}$, we can write the *dyadic Green's tensor* as

$$\begin{aligned}\overleftrightarrow{\mathbf{G}}(\mathbf{r}, \mathbf{r}') &= \left[1 + \frac{1}{k^2}\nabla\nabla\cdot\right] g(\mathbf{r}, \mathbf{r}')\,(\hat{\mathbf{x}}\hat{\mathbf{x}} + \hat{\mathbf{y}}\hat{\mathbf{y}} + \hat{\mathbf{z}}\hat{\mathbf{z}}) \\ &= \left[1 + \frac{1}{k^2}\nabla\nabla\cdot\right] g(\mathbf{r}, \mathbf{r}')\,\overleftrightarrow{\mathbf{I}} \\ &= \left[\overleftrightarrow{\mathbf{I}} + \frac{1}{k^2}\nabla\nabla\right] g(\mathbf{r}, \mathbf{r}')\,, \end{aligned} \tag{2.60}$$

where $\nabla \cdot \left[g\overleftrightarrow{\mathbf{I}}\right] = \nabla g$ has been used in the last equality. [5]
Due to the double derivative of the scalar Green's function, the dyadic Green's tensor is strongly singular and numerical evaluation via integration can be problematic when observation points are close to the source points. There are methods of handling the singularities, such as *singularity extraction* techniques where the singular integral is extracted and calculated in closed form. [8]

2.3 GREEN'S TENSOR IN CYLINDRICAL COORDINATES

In this section, the dyadic Green's tensor will be rewritten into cylindrical coordinates. In the following subsections, the derivation of the Green's tensor for a planar interface of two media will made, and expressions for the far-field Green's tensor are obtained. This section is largely based on [9].

When solving electromagnetic problems it is sometimes advantageous to change to a different coordinate system. In the case of the dyadic Green's tensor, changing from Cartesian coordinates to cylindrical coordinates allows for the fields to be represented as a single integral, making implementation easier. We first make use of Weyl's identity, presented in [10], to obtain an angular spectrum representation of Eq. (2.50):

$$g(\mathbf{r}, \mathbf{r}') = \frac{i}{8\pi^2}\int\limits_{k_x}\int\limits_{k_y} \frac{1}{k_{z_1}} e^{ik_x(x-x')} e^{ik_y(y-y')} e^{ik_{z_1}|z-z'|}\, dk_x dk_y\,, \tag{2.61}$$

where the subscript "1" refers to a parameters value in medium 1.
In order to convert to cylindrical coordinates, we define

$$x - x' = \rho_r \cos\phi_r\,, \tag{2.62a}$$
$$y - y' = \rho_r \sin\phi_r \tag{2.62b}$$
$$k_x = k_1 \cos\phi_k\,, \tag{2.62c}$$
$$k_y = k_1 \sin\phi_k\,, \tag{2.62d}$$

where it should be noted that ρ_r and ϕ_r are defined with respect to the relative distance, hence the subscript r.
By using Eqs. (2.62), one can express Eq. (2.61) in cylindrical coordinates as

$$g(\mathbf{r}, \mathbf{r}') = \frac{i}{8\pi^2} \iint \frac{1}{k_{z_1}} e^{ik_\rho \rho_r \cos(\phi_k - \phi_r)} e^{ik_{z_1}|z-z'|} \, k_\rho dk_\rho d\phi_k \,. \tag{2.63}$$

By using the Bessel function given by

$$J_0(\alpha) = \frac{1}{2\pi} \int_0^{2\pi} e^{i\alpha \cos\phi} \, d\phi \,, \tag{2.64}$$

the scalar Green's function can be rewritten as

$$g(\mathbf{r}, \mathbf{r}') = \frac{i}{4\pi} \int \frac{k_\rho}{k_{z_1}} J_0(k_\rho \rho_r) e^{ik_{z_1}|z-z'|} \, dk_\rho \,. \tag{2.65}$$

By using the gradient i cylindrical coordinates $\left(\nabla = \hat{\boldsymbol{\rho}}_r \frac{\partial}{\partial \rho_r} + \hat{\boldsymbol{\phi}}_r \frac{1}{\rho_r} \frac{\partial}{\partial \phi_r} + \hat{\mathbf{z}} \frac{\partial}{\partial z}\right)$, the gradient of the Green's function can be expressed as

$$\begin{aligned} \nabla g(\mathbf{r}, \mathbf{r}') = \frac{i}{4\pi} \int \left\{ \hat{\boldsymbol{\rho}}_r \, k_\rho J_0'(k_\rho \rho_r) + \hat{\mathbf{z}} \, ik_{z_1} \frac{z - z'}{|z - z'|} J_0(k_\rho \rho_r) \right\} & \\ \times \, \frac{k_\rho}{k_{z_1}} e^{ik_{z_1}|z-z'|} \, dk_\rho \,, & \end{aligned} \tag{2.66}$$

where the factor $\frac{z-z'}{|z-z'|}$ accounts for either $z' > z$ or $z' < z$.
Additionally taking the gradient of Eq. (2.66) yields

$$\begin{aligned} \nabla\nabla g(\mathbf{r}, \mathbf{r}') = \frac{i}{4\pi} \int \Big\{ & \hat{\boldsymbol{\rho}}_r \hat{\boldsymbol{\rho}}_r \, k_\rho^2 J_0''(k_\rho \rho_r) + (\hat{\boldsymbol{\rho}}_r \hat{\mathbf{z}} + \hat{\mathbf{z}} \hat{\boldsymbol{\rho}}_r) \, ik_\rho k_{z_1} \frac{z - z'}{|z - z'|} J_0'(k_\rho \rho_r) \\ & + \hat{\boldsymbol{\phi}}_r \hat{\boldsymbol{\phi}}_r \, \frac{k_\rho}{\rho_r} J_0'(k_\rho \rho_r) - \hat{\mathbf{z}}\hat{\mathbf{z}} \, k_{z_1}^2 \, J_0(k_\rho \rho_r) \Big\} \, \frac{k_\rho}{k_{z_1}} e^{ik_{z_1}|z-z'|} \, dk_\rho \,. \end{aligned} \tag{2.67}$$

It should again be noted that the cylindrical unit vectors $\left(\hat{\boldsymbol{\rho}}_r, \hat{\boldsymbol{\phi}}_r, \hat{\mathbf{z}}\right)$ are relative, and defined by

$$\hat{\boldsymbol{\rho}}_r = \hat{\mathbf{x}} \, \cos\phi_r + \hat{\mathbf{y}} \, \sin\phi_r \,, \tag{2.68a}$$

$$\hat{\boldsymbol{\phi}}_r = -\hat{\mathbf{x}} \, \sin\phi_r + \hat{\mathbf{y}} \, \cos\phi_r \,, \tag{2.68b}$$

where ϕ_r is the relative angle defined in (2.62). By substituting Eq. (2.67) into the dyadic Green's tensor, given by Eq. (2.60), we obtain an expression for the free-space dyadic Green's tensor in cylindrical coordinates:

$$\begin{aligned}
\overleftrightarrow{\mathbf{G}}(\mathbf{r},\mathbf{r}') = \frac{i}{4\pi}\int \Bigg\{ & \hat{\boldsymbol{\rho}}_r\hat{\boldsymbol{\rho}}_r \left[J_0(k_\rho\rho_r) + \frac{k_\rho^2}{k_1^2} J_0''(k_\rho\rho_r)\right] + \hat{\mathbf{z}}\hat{\mathbf{z}} \left[1 - \frac{k_{z_1}^2}{k_1^2}\right] J_0(k_\rho\rho_r) \\
& + \hat{\boldsymbol{\phi}}_r\hat{\boldsymbol{\phi}}_r \left[J_0(k_\rho\rho_r) + \frac{k_\rho}{k_1^2\rho_r} J_0'(k_\rho\rho_r)\right] + (\hat{\boldsymbol{\rho}}_r\hat{\mathbf{z}} + \hat{\mathbf{z}}\hat{\boldsymbol{\rho}}_r)\, i\frac{k_\rho k_{z_1}}{k_1^2}\frac{z-z'}{|z-z'|} J_0'(k_\rho\rho_r)\Bigg\} \\
& \times \frac{k_\rho}{k_{z_1}} e^{ik_{z_1}|z-z'|}\, dk_\rho \\
= \frac{i}{4\pi}\int \Bigg\{ & \hat{\boldsymbol{\rho}}_r\hat{\boldsymbol{\rho}}_r \left[J_0(k_\rho\rho_r) + \frac{k_\rho^2}{k_1^2} J_0''(k_\rho\rho_r)\right] + \hat{\mathbf{z}}\hat{\mathbf{z}} \frac{k_\rho^2}{k_1^2} J_0(k_\rho\rho_r) \\
& + \hat{\boldsymbol{\phi}}_r\hat{\boldsymbol{\phi}}_r \left[J_0(k_\rho\rho_r) + \frac{k_\rho^2}{k_1^2}\frac{J_0'(k_\rho\rho_r)}{k_\rho\rho_r}\right] + (\hat{\boldsymbol{\rho}}_r\hat{\mathbf{z}} + \hat{\mathbf{z}}\hat{\boldsymbol{\rho}}_r)\, i\frac{k_\rho k_{z_1}}{k_1^2}\frac{z-z'}{|z-z'|} J_0'(k_\rho\rho_r)\Bigg\} \\
& \times \frac{k_\rho}{k_{z_1}} e^{ik_{z_1}|z-z'|}\, dk_\rho\,. \qquad (2.69)
\end{aligned}$$

where $\overleftrightarrow{\mathbf{I}} = \hat{\mathbf{x}}\hat{\mathbf{x}} + \hat{\mathbf{y}}\hat{\mathbf{y}} + \hat{\mathbf{z}}\hat{\mathbf{z}} = \hat{\boldsymbol{\rho}}\hat{\boldsymbol{\rho}} + \hat{\boldsymbol{\phi}}\hat{\boldsymbol{\phi}} + \hat{\mathbf{z}}\hat{\mathbf{z}}$ has been used.
In the remaining sections of this thesis, Eq. (2.69) will be referred to as the *direct Green's tensor*, denoted by $\overleftrightarrow{\mathbf{G}}^{(d)}(\mathbf{r},\mathbf{r}')$.

2.3.1 *Green's Tensor for a Planar Interface*

For scattering near an interface one must account for reflection and transmission in order to describe the electric field in both media. It is therefore needed to consider both s- and p-polarized light when constructing the dyadic Green's tensor for a two-layered planar interface. The following dot-products between Cartesian- and cylindrical coordinates will be utilized in the derivation:

$$\hat{\boldsymbol{\rho}}_r \cdot \hat{\mathbf{x}} = \cos\phi_r\,, \qquad (2.70a)$$

$$\hat{\boldsymbol{\rho}}_r \cdot \hat{\mathbf{y}} = \sin\phi_r\,, \qquad (2.70b)$$

$$\hat{\boldsymbol{\phi}}_r \cdot \hat{\mathbf{x}} = -\sin\phi_r\,, \qquad (2.70c)$$

$$\hat{\boldsymbol{\phi}}_r \cdot \hat{\mathbf{y}} = \cos\phi_r\,. \qquad (2.70d)$$

Consider a planar structure with interface located at $z = 0$. For $z > 0$, the Green's tensor can be decomposed into two parts; the *direct Green tensor* given by Eq. (2.69), and an *indirect Green tensor* that deals with the reflection that occurs due to the surface. For $z < 0$, a *transmitted Green's tensor* have to be used. For a two-layered planer interface, this is expressed by

$$\overleftrightarrow{\mathbf{G}}(\mathbf{r},\mathbf{r}') = \begin{cases} \overleftrightarrow{\mathbf{G}}^{(d)}(\mathbf{r},\mathbf{r}') + \overleftrightarrow{\mathbf{G}}^{(i)}(\mathbf{r},\mathbf{r}'), & z > 0, z' > 0\,, \\ \overleftrightarrow{\mathbf{G}}^{(t)}(\mathbf{r},\mathbf{r}'), & z < 0, z > 0\,. \end{cases} \qquad (2.71)$$

We will only consider a planer interface between two isotropic media, and so the permittivity ε will be given by

$$\varepsilon(\mathbf{r}) = \begin{cases} \varepsilon_1, & z > 0\,, \\ \varepsilon_2, & z < 0\,. \end{cases} \tag{2.72}$$

In order to find how the appropriate Green's tensors can be expressed, we make use of the unit dyadic $\overleftrightarrow{\mathbf{I}}$, which has the property

$$\begin{aligned} \overleftrightarrow{\mathbf{G}} &= \overleftrightarrow{\mathbf{G}} \cdot \overleftrightarrow{\mathbf{I}} = \overleftrightarrow{\mathbf{G}} \cdot (\hat{\mathbf{x}}\hat{\mathbf{x}} + \hat{\mathbf{y}}\hat{\mathbf{y}} + \hat{\mathbf{z}}\hat{\mathbf{z}}) \\ &= \left(\overleftrightarrow{\mathbf{G}} \cdot \hat{\mathbf{x}}\right)\hat{\mathbf{x}} + \left(\overleftrightarrow{\mathbf{G}} \cdot \hat{\mathbf{y}}\right)\hat{\mathbf{y}} + \left(\overleftrightarrow{\mathbf{G}} \cdot \hat{\mathbf{z}}\right)\hat{\mathbf{z}}\,. \end{aligned} \tag{2.73}$$

We start by considering the $\hat{\mathbf{z}}$-component of an electric field incident on the planar surface, where $z' > z > 0$, given by

$$\begin{aligned} \mathbf{E}_{i,z}(\mathbf{r}) &= \overleftrightarrow{\mathbf{G}}^{(d)}(\mathbf{r}, \mathbf{r}') \cdot \hat{\mathbf{z}} \\ &= \frac{i}{4\pi} \int_0^\infty \left\{ \hat{\mathbf{z}}\, \frac{k_\rho^2}{k_1^2} J_0(k_\rho \rho_r) - \hat{\boldsymbol{\rho}}_r\, i \frac{k_\rho k_{z_1}}{k_1^2} J_0'(k_\rho \rho_r) \right\} \frac{k_\rho}{k_{z_1}} e^{ik_{z_1}|z-z'|}\, dk_\rho\,. \end{aligned} \tag{2.74}$$

The $\hat{\mathbf{z}}$-component of the reflected and transmitted fields can thus be expressed by

$$\begin{aligned} \mathbf{E}_{r,z} = \frac{i}{4\pi} \int_0^\infty r^{(p)}(k_\rho) & \left\{ \hat{\mathbf{z}}\, \frac{k_\rho^2}{k_1^2} J_0(k_\rho \rho_r) + \hat{\boldsymbol{\rho}}_r\, i \frac{k_\rho k_{z_1}}{k_1^2} J_0'(k_\rho \rho_r) \right\} \\ & \times \frac{k_\rho}{k_{z_1}} e^{ik_{z_1}(z+z')}\, dk_\rho\,, \end{aligned} \tag{2.75}$$

$$\begin{aligned} \mathbf{E}_{t,z} = \frac{i}{4\pi} \int_0^\infty t^{(p)}(k_\rho)\, \frac{\varepsilon_1}{\varepsilon_2} & \left\{ \hat{\mathbf{z}}\, \frac{k_\rho^2}{k_1^2} J_0(k_\rho \rho_r) - \hat{\boldsymbol{\rho}}_r\, i \frac{k_\rho k_{z_1}}{k_1^2} J_0'(k_\rho \rho_r) \right\} \\ & \times \frac{k_\rho}{k_{z_1}} e^{ik_{z_1} z'} e^{-ik_{z_2} z}\, dk_\rho\,, \end{aligned} \tag{2.76}$$

where $r^{(p)}$ and $t^{(p)}$ are the Fresnel reflection and transmission coefficients defined by

$$r^{(p)}(k_\rho) = \frac{\varepsilon_2 k_{z_1} - \varepsilon_1 k_{z_2}}{\varepsilon_2 k_{z_1} + \varepsilon_1 k_{z_2}}\,, \tag{2.77a}$$

$$t^{(p)}(k_\rho) = 1 + r^{(p)}(k_\rho)\,, \tag{2.77b}$$

where (p) refers to p-polarized components, and the subscripts, "1" and "2", refers to medium 1 and medium 2, respectively. By using Eqs. (2.70), the $\hat{\mathbf{x}}$- and

$\hat{\mathbf{y}}$-components of the incident electric field can be calculated as

$$\mathbf{E}_{i,x} = \overleftrightarrow{\mathbf{G}}^{(d)}(\mathbf{r},\mathbf{r}') \cdot \hat{\mathbf{x}} \tag{2.78}$$

$$= \frac{i}{4\pi}\int_0^\infty \left\{ \hat{\boldsymbol{\rho}}_r \cos\phi_r \left[J_0(k_\rho\rho_r) + \frac{k_\rho^2}{k_1^2} J_0''(k_\rho\rho_r) \right] - \hat{\boldsymbol{\phi}}_r \sin\phi_r \left[J_0(k_\rho\rho_r) + \frac{k_\rho^2}{k_1^2}\frac{J_0'(k_\rho\rho_r)}{k_\rho\rho_r} \right] - \hat{\mathbf{z}}\, i\frac{k_\rho k_{z_1}}{k_1^2} J_0'(k_\rho\rho_r)\cos\phi_r \right\} \frac{k_\rho}{k_{z_1}} e^{ik_{z_1}(z'-z)}\, dk_\rho$$

$$= \frac{i}{4\pi}\int_0^\infty \left\{ -\hat{\boldsymbol{\rho}}_r \cos\phi_r \left[\frac{J_0'(k_\rho\rho_r)}{k_\rho\rho_r} + \frac{k_{z_1}^2}{k_1^2} J_0''(k_\rho\rho_r) \right] + \hat{\boldsymbol{\phi}}_r \sin\phi_r \left[J_0''(k_\rho\rho_r) + \frac{k_{z_1}^2}{k_1^2}\frac{J_0'(k_\rho\rho_r)}{k_\rho\rho_r} \right] - \hat{\mathbf{z}}\, i\frac{k_{z_1} k_\rho}{k_1^2} J_0'(k_\rho\rho_r)\cos\phi_r \right\} \frac{k_\rho}{k_{z_1}} e^{ik_{z_1}(z'-z)}\, dk_\rho\,,$$

and

$$\mathbf{E}_{i,y} = \overleftrightarrow{\mathbf{G}}^{(d)}(\mathbf{r},\mathbf{r}') \cdot \hat{\mathbf{y}} \tag{2.79}$$

$$= \frac{i}{4\pi}\int_0^\infty \left\{ \hat{\boldsymbol{\rho}}_r \sin\phi_r \left[J_0(k_\rho\rho_r) + \frac{k_\rho^2}{k_1^2} J_0''(k_\rho\rho_r) \right] + \hat{\boldsymbol{\phi}}_r \cos\phi_r \left[J_0(k_\rho\rho_r) + \frac{k_\rho^2}{k_1^2}\frac{J_0'(k_\rho\rho_r)}{k_\rho\rho_r} \right] - \hat{\mathbf{z}}\, i\frac{k_\rho k_{z_1}}{k_1^2} J_0'(k_\rho\rho_r)\sin\phi_r \right\} \frac{k_\rho}{k_{z_1}} e^{ik_{z_1}(z'-z)}\, dk_\rho$$

$$= \frac{i}{4\pi}\int_0^\infty \left\{ -\hat{\boldsymbol{\rho}}_r \sin\phi_r \left[\frac{J_0'(k_\rho\rho_r)}{k_\rho\rho_r} + \frac{k_{z_1}^2}{k_1^2} J_0''(k_\rho\rho_r) \right] - \hat{\boldsymbol{\phi}}_r \cos\phi_r \left[J_0''(k_\rho\rho_r) + \frac{k_{z_1}^2}{k_1^2}\frac{J_0'(k_\rho\rho_r)}{k_\rho\rho_r} \right] - \hat{\mathbf{z}}\, i\frac{k_\rho k_{z_1}}{k_1^2} J_0'(k_\rho\rho_r)\sin\phi_r \right\} \frac{k_\rho}{k_{z_1}} e^{ik_{z_1}(z'-z)}\, dk_\rho\,.$$

The components of the incident electric field given by Eqs. (2.78) and (2.79) can be separated into s- and p-polarized components:

$$\mathbf{E}_{i,x}^{(s)}(\mathbf{r}) = \frac{i}{4\pi}\int_0^\infty \left\{ \hat{\boldsymbol{\phi}}_r\, J_0''(k_\rho\rho_r)\sin\phi - \hat{\boldsymbol{\rho}}_r \frac{J_0'(k_\rho\rho_r)}{k_\rho\rho_r}\cos\phi_r \right\} \times \frac{k_\rho}{k_{z_1}} e^{ik_{z_1}(z'-z)}\, dk_\rho\,, \tag{2.80}$$

$$\mathbf{E}_{i,x}^{(p)}(\mathbf{r}) = \frac{i}{4\pi}\int_0^\infty \left\{ \hat{\boldsymbol{\phi}}_r \frac{k_{z_1}^2}{k_1^2}\frac{J_0'(k_\rho\rho_r)}{k_\rho\rho_r} - \hat{\boldsymbol{\rho}}_r \frac{k_{z_1}^2}{k_1^2} J_0''(k_\rho\rho_r)\cos\phi_r - \hat{\mathbf{z}}\, i\frac{k_\rho k_{z_1}}{k_1^2} J_0'(k_\rho\rho_r)\cos\phi_r \right\} \frac{k_\rho}{k_{z_1}} e^{ik_{z_1}(z'-z)}\, dk_\rho\,, \tag{2.81}$$

and

$$\mathbf{E}_{i,y}^{(s)}(\mathbf{r}) = \frac{i}{4\pi}\int_0^\infty \left\{-\hat{\boldsymbol{\rho}}_r \,\frac{J_0'(k_\rho\rho_r)}{k_\rho\rho_r}\sin\phi_r - \hat{\boldsymbol{\phi}}_r\, J_0''(k_\rho\rho_r)\cos\phi_r\right\} \times \frac{k_\rho}{k_{z_1}} e^{ik_{z_1}(z'-z)}\,dk_\rho\,, \tag{2.82}$$

$$\mathbf{E}_{i,y}^{(p)}(\mathbf{r}) = \frac{i}{4\pi}\int_0^\infty \left\{-\hat{\boldsymbol{\rho}}_r \,\frac{k_{z_1}^2}{k_1^2} J_0''(k_\rho\rho_r)\sin\phi_r - \hat{\boldsymbol{\phi}}_r\, \frac{k_{z_1}^2}{k_1^2}\frac{J_0'(k_\rho\rho_r)}{k_\rho\rho_r}\cos\phi_r - \hat{\mathbf{z}}\, i\frac{k_\rho k_{z_1}}{k_1^2} J_0'(k_\rho\rho_r)\sin\phi_r\right\} \frac{k_\rho}{k_{z_1}} e^{ik_{z_1}(z'-z)}\,dk_\rho\,. \tag{2.83}$$

The s- and p-polarized components of the reflected field for the $\hat{\mathbf{x}}$- and $\hat{\mathbf{y}}$-components are then given by

$$\mathbf{E}_{r,x}^{(s)} = \frac{i}{4\pi}\int_0^\infty \left\{-\hat{\boldsymbol{\rho}}_r \,\frac{J_0'(k_\rho\rho_r)}{k_\rho\rho_r}\cos\phi + \hat{\boldsymbol{\phi}}_r\, J_0''(k_\rho\rho_r)\sin\phi_r\right\} r^{(s)}(k_\rho) \times \frac{k_\rho}{k_{z_1}} e^{ik_{z_1}(z+z')}\,dk_\rho\,, \tag{2.84}$$

$$\mathbf{E}_{r,x}^{(p)} = \frac{i}{4\pi}\int_0^\infty \left\{\hat{\boldsymbol{\rho}}_r \,\frac{k_{z_1}^2}{k_1^2} J_0''(k_\rho\rho_r)\cos\phi_r - \hat{\boldsymbol{\phi}}\_r,\, \frac{k_{z_1}^2}{k_1^2}\frac{J_0'(k_\rho\rho_r)}{k_\rho\rho_r}\sin\phi_r - \hat{\mathbf{z}}\, i\frac{k_\rho k_{z_1}}{k_1^2} J_0'(k_\rho\rho_r)\cos\phi_r\right\} r^{(p)}(k_\rho)\frac{k_\rho}{k_{z_1}} e^{ik_{z_1}(z+z')}\,dk_\rho\,, \tag{2.85}$$

and

$$\mathbf{E}_{r,y}^{(s)} = \frac{i}{4\pi}\int_0^\infty \left\{-\hat{\boldsymbol{\rho}} \,\frac{J_0'(k_\rho\rho)}{k_\rho\rho}\sin\phi - \hat{\boldsymbol{\phi}}\, J_0''(k_\rho\rho)\cos\phi\right\} r^{(s)}(k_\rho) \times \frac{k_\rho}{k_{z_1}} e^{ik_{z_1}(z+z')}\,dk_\rho\,, \tag{2.86}$$

$$\mathbf{E}_{r,y}^{(p)} = \frac{i}{4\pi}\int_0^\infty \left\{\hat{\boldsymbol{\rho}}_r \,\frac{k_{z_1}^2}{k_1^2} J_0''(k_\rho\rho_r)\sin\phi_R + \hat{\boldsymbol{\phi}}_r\, \frac{k_{z_1}^2}{k_1^2}\frac{J_0'(k_\rho\rho_r)}{k_\rho\rho_r}\cos\phi_r - \hat{\mathbf{z}}\, i\frac{k_\rho k_{z_1}}{k_1^2} J_0'(k_\rho\rho_r)\sin\phi_r\right\} r^{(p)}(k_\rho)\frac{k_\rho}{k_{z_1}} e^{ik_{z_1}(z+z')}\,dk_\rho\,, \tag{2.87}$$

where the reflection and transmission coefficients for s-polerization are given by

$$r^{(s)}(k_\rho) = \frac{k_{z_1} - k_{z_2}}{k_{z_1} + k_{z_2}}\,, \tag{2.88a}$$

$$t^{(s)}(k_\rho) = 1 + r^{(s)}(k_\rho)\,. \tag{2.88b}$$

By combining the s- and p-polarized components for each $\hat{\mathbf{x}}$, $\hat{\mathbf{y}}$ and $\hat{\mathbf{z}}$ component of the reflected field, we can obtain the indirect Green's tensor:

$$\overleftrightarrow{\mathbf{G}}^{(i)}(\mathbf{r},\mathbf{r}') = \mathbf{E}_{r,x}\,\hat{\mathbf{x}} + \mathbf{E}_{r,y}\,\hat{\mathbf{y}} + \mathbf{E}_{r,z}\,\hat{\mathbf{z}}\,, \tag{2.89}$$

where

$$\mathbf{E}_{r,x} = \mathbf{E}^{(s)}_{r,x} + \mathbf{E}^{(p)}_{r,x}\,, \tag{2.90a}$$

$$\mathbf{E}_{r,y} = \mathbf{E}^{(s)}_{r,y} + \mathbf{E}^{(p)}_{r,y}\,, \tag{2.90b}$$

$$\mathbf{E}_{r,z} = \mathbf{E}^{(p)}_{r,z}\,. \tag{2.90c}$$

The Cartesian unit vectors can be expressed in terms of the cylindrical unit vectors as

$$\hat{\mathbf{x}} = \hat{\boldsymbol{\rho}}_r\,\cos\phi_r - \hat{\boldsymbol{\phi}}_r\,\sin\phi_r\,, \tag{2.91a}$$

$$\hat{\mathbf{y}} = \hat{\boldsymbol{\rho}}_r\,\sin\phi_r + \hat{\boldsymbol{\phi}}_r\,\cos\phi\,, \tag{2.91b}$$

which allows for Eq. (2.89) to be written more compact as

$$\begin{aligned}
\overleftrightarrow{\mathbf{G}}^{(i)}(\mathbf{r},\mathbf{r}') = \frac{i}{4\pi}\int_0^\infty \Bigg\{ &- r^{(s)}(k_\rho)\left(\hat{\boldsymbol{\rho}}_r\hat{\boldsymbol{\rho}}_r\,\frac{J_0'(k_\rho\rho_r)}{k_\rho\rho_r} + \hat{\boldsymbol{\phi}}_r\hat{\boldsymbol{\phi}}_r\,J_0''(k_\rho\rho_r)\right) \\
&+ r^{(p)}(k_\rho)\left(\hat{\boldsymbol{\rho}}_r\hat{\boldsymbol{\rho}}_r\,\frac{k_{z_1}^2}{k_1^2}\,J_0''(k_\rho\rho_r) + \hat{\boldsymbol{\phi}}_r\hat{\boldsymbol{\phi}}_r\,\frac{k_{z_1}^2}{k_1^2}\,\frac{J_0'(k_\rho\rho_r)}{k_\rho\rho_r} + \hat{\mathbf{z}}\hat{\mathbf{z}}\,\frac{k_\rho^2}{k_1^2}\,J_0(k_\rho\rho_r)\right. \\
&\left. + (\hat{\boldsymbol{\rho}}_r\hat{\mathbf{z}} - \hat{\mathbf{z}}\hat{\boldsymbol{\rho}}_r)\,i\frac{k_\rho k_{z_1}}{k_1^2}\,J_0'(k_\rho\rho_r)\right)\Bigg\}\,\frac{k_\rho}{k_{z_1}}e^{ik_{z_1}(z+z')}\,dk_\rho\,.
\end{aligned} \tag{2.92}$$

In a similar manner as done for Eq. (2.89), the transmitted Green's tensor can be obtained by

$$\overleftrightarrow{\mathbf{G}}^{(t)}(\mathbf{r},\mathbf{r}') = \mathbf{E}_{t,x}\,\hat{\mathbf{x}} + \mathbf{E}_{t,y}\,\hat{\mathbf{y}} + \mathbf{E}_{t,z}\,\hat{\mathbf{z}}\,, \tag{2.93}$$

where

$$\mathbf{E}_{t,x} = \mathbf{E}^{(s)}_{t,x} + \mathbf{E}^{(p)}_{t,x}\,, \tag{2.94a}$$

$$\mathbf{E}_{t,y} = \mathbf{E}^{(s)}_{t,y} + \mathbf{E}^{(p)}_{t,y}\,, \tag{2.94b}$$

$$\mathbf{E}_{t,z} = \mathbf{E}^{(p)}_{t,z}\,. \tag{2.94c}$$

The s- and p-polarized terms of Eqs. (2.94a) and (2.94b) are given by

$$\mathbf{E}^{(s)}_{t,x} = \frac{i}{4\pi}\int_0^\infty \left\{ -\hat{\boldsymbol{\rho}}_r \frac{J_0'(k_\rho\rho_r)}{k_\rho\rho_r}\cos\phi_r + \hat{\boldsymbol{\phi}}_r J_0''(k_\rho\rho_r)\sin\phi_r \right\} t^{(s)}(k_\rho) \times \frac{k_\rho}{k_{z_1}} e^{ik_{z_1}z'} e^{-ik_{z_2}z}\, dk_\rho\,, \tag{2.95}$$

$$\mathbf{E}^{(p)}_{t,x} = \frac{i}{4\pi}\int_0^\infty \left\{ -\hat{\boldsymbol{\rho}}_r \frac{k_{z_1}k_{z_2}}{k_1^2} J_0''(k_\rho\rho_r)\cos\phi_r + \hat{\boldsymbol{\phi}}_r \frac{k_{z_1}k_{z_2}}{k_1^2}\frac{J_0'(k_\rho\rho_r)}{k_\rho\rho_r}\sin\phi_r - \hat{\mathbf{z}}\, i\frac{k_\rho k_{z_1}}{k_1^2} J_0'(k_\rho\rho_r)\cos\phi_r \right\} t^{(p)}(k_\rho)\frac{k_\rho}{k_{z_1}} e^{ik_{z_1}z'} e^{-ik_{z_2}z}\, dk_\rho\,, \tag{2.96}$$

$$\mathbf{E}^{(s)}_{t,y} = \frac{i}{4\pi}\int_0^\infty \left\{ -\hat{\boldsymbol{\rho}}_r \frac{J_0'(k_\rho\rho_r)}{k_\rho\rho_r}\sin\phi_r - \hat{\boldsymbol{\phi}}_r J_0''(k_\rho\rho_r)\cos\phi_r \right\} t^{(s)}(k_\rho) \times \frac{k_\rho}{k_{z_1}} e^{ik_{z_1}z'} e^{-ik_{z_2}z}\, dk_\rho\,, \tag{2.97}$$

$$\mathbf{E}^{(p)}_{t,y} = \frac{i}{4\pi}\int_0^\infty \left\{ -\hat{\boldsymbol{\rho}}_r \frac{k_{z_1}k_{z_2}}{k_1^2} J_0''(k_\rho\rho_r)\sin\phi_r - \hat{\boldsymbol{\phi}} \frac{k_{z_1}k_{z_2}}{k_1^2}\frac{J_0'(k\rho\rho)}{k_\rho\rho}\cos\phi_r - \hat{\mathbf{z}}\, i\frac{k_\rho k_{z_1}}{k_1^2} J_0'(k_\rho\rho_r)\sin\phi_r \right\} t^{(p)}(k_\rho)\frac{k_\rho}{k_{z_1}} e^{ik_{z_1}z'} e^{-ik_{z_2}z}\, dk_\rho\,. \tag{2.98}$$

Again we convert the Cartesian unit vectors to cylindrical unit vectors, and thereby obtain the transmitted Green's tensor given by

$$\overleftrightarrow{\mathbf{G}}^{(t)}(\mathbf{r},\mathbf{r}') = \frac{i}{4\pi}\int_0^\infty \Bigg\{ - t^{(s)}(k_\rho)\left(\hat{\boldsymbol{\rho}}_r\hat{\boldsymbol{\rho}}_r \frac{J_0'(k_\rho\rho_r)}{k_\rho\rho_r} - \hat{\boldsymbol{\phi}}_r\hat{\boldsymbol{\phi}}_r J_0''(k_\rho\rho_r)\right) - t^{(p)}(k_\rho)\Bigg(\hat{\boldsymbol{\rho}}_r\hat{\boldsymbol{\rho}}_r \frac{k_{z_1}k_{z_2}}{k_1^2}J_0''(k_\rho\rho_r) + \hat{\boldsymbol{\phi}}_r\hat{\boldsymbol{\phi}}_r \frac{k_{z_1}k_{z_2}}{k_1^2}\frac{J_0'(k_\rho\rho_r)}{k_\rho\rho_r} + \hat{\mathbf{z}}\hat{\mathbf{z}}\frac{k_\rho^2}{k_1^2}J_0(k_\rho\rho_r) -(\hat{\boldsymbol{\rho}}_r\hat{\mathbf{z}}\frac{k_{z_2}}{k_{z_1}} + \hat{\mathbf{z}}\hat{\boldsymbol{\rho}}_r)\, i\frac{k_\rho k_{z_1}}{k_1^2}J_0'(k_\rho\rho_r)\Bigg)\Bigg\} \frac{k_\rho}{k_{z_1}} e^{ik_{z_1}z'} e^{-ik_{z_2}z}\, dk_\rho\,. \tag{2.99}$$

The Green's tensor for a planer interface is given by Eqs. (2.69), (2.92) and (2.99). The three equations are also included in Appendix A for easier overview.

2.3.2 *Far-Field Green's Tensor*

If we want to calculate the far-field radiation, the Green's tensor can be expressed by simpler equations, making implementation easier. We will for that reason derive the far-field Green's tensor. We start by considering the $\hat{\boldsymbol{\phi}}\hat{\boldsymbol{\phi}}$ term of s-polarized part of the indirect Green's tensor:

$$\overleftrightarrow{\mathbf{G}}^{(i,ff)}_{\phi\phi} = -\frac{i}{4\pi}\int_0^\infty \frac{k_\rho}{k_{z_1}} J_0''(k_\rho\rho_r) e^{ik_{z_1}(z+z')}\, dk_\rho\,. \tag{2.100}$$

By using the relation

$$J_0''(x) = -J_0(x) - \frac{1}{x}J_0'(x)\,, \tag{2.101}$$

one can separate Eq. (2.100) into two integrals:

$$\mathcal{I}_1 = \frac{i}{4\pi}\int_0^\infty \frac{k_\rho}{k_{z_1}} J_0(k_\rho\rho_r) e^{ik_{z_1}(z+z')}\,dk_\rho\,, \tag{2.102a}$$

$$\mathcal{I}_2 = \frac{i}{4\pi}\int_0^\infty \frac{k_\rho}{k_{z_1}}\frac{1}{k_\rho\rho_r} J_0'(k_\rho\rho_r) e^{ik_{z_1}(z+z')}\,dk_\rho\,. \tag{2.102b}$$

In the far-field limit $\hat{\boldsymbol{\rho}}_r \approx \hat{\boldsymbol{\rho}}$ and $\hat{\boldsymbol{\phi}}_r \approx \hat{\boldsymbol{\phi}}$, and since the $1/\rho_r$-term will make the $\mathcal{I}_2$-integral vanish, we only need to consider Eq. (2.102a). The same holds true for other integrals in Eq. (2.92) which contain a $1/\rho_r$-term. For $k_\rho > k_1$, the exponential term $e^{ik_{z_1}z}$ will approach zero for large values of z, since k_{z_1} becomes imaginary. This holds for all the integrals in Eq. (2.92), and all of them therefore only need to be evaluated for $0 \leq k_\rho \leq k_1$ when considering the far-field approximation. By using

$$k_{z_1} = k_1\cos\alpha\,, \tag{2.103a}$$

$$k_\rho = k_1\sin\alpha\,, \tag{2.103b}$$

we can express Eq. (2.100) as

$$\overleftrightarrow{\mathbf{G}}^{(i,ff)}_{\phi\phi} \approx \frac{i}{4\pi}\int_{\alpha=0}^{\pi/2} k_\rho J_0(k_\rho\rho_r) e^{ik_{z_1}(z+z')}\,d\alpha\,. \tag{2.104}$$

Next, we will also use that

$$\rho = r\cos\theta\,, \tag{2.105a}$$

$$z = r\sin\theta\,, \tag{2.105b}$$

where ρ is the regular cylindrical coordinate, and $0 \leq \theta \leq \pi/2$.
When $\mathbf{r}'$ is near the origin and the observation point $\mathbf{r}$ is far away, the approximation $\rho_r \approx \rho - \mathbf{r}'\cdot\hat{\boldsymbol{\rho}}$ can be made, and by applying that

$$J_0(x) \approx \sqrt{\frac{2}{x\pi}}\cos(x-\pi/4) \quad \text{for} \quad x \gg 1\,, \tag{2.106}$$

we can write the following expression:

$$\begin{aligned}
\cos(k_\rho\rho_r - \pi/4)e^{ik_{z_1}z} &= \frac{1}{2}\left[e^{i(k_\rho\rho_r-\pi/4)} + e^{-i(k_\rho\rho_r-\pi/4)}\right]e^{ik_{z_1}z} \\
&\approx \frac{1}{2}\left[e^{ik_\rho\rho}e^{-k_\rho\mathbf{r}'\cdot\hat{\boldsymbol{\rho}}}e^{-\pi/4} + e^{-ik_\rho\rho}e^{k_\rho\mathbf{r}'\cdot\hat{\boldsymbol{\rho}}}e^{\pi/4}\right]e^{ik_{z_1}z} \\
&= \frac{1}{2}\left[e^{ik_1r\cos(\alpha-\theta)}e^{-k_\rho\mathbf{r}'\cdot\hat{\boldsymbol{\rho}}}e^{-\pi/4} + e^{ik_1r\cos(\alpha+\theta)}e^{k_\rho\mathbf{r}'\cdot\hat{\boldsymbol{\rho}}}e^{\pi/4}\right],
\end{aligned} \tag{2.107}$$

where $\cos(\alpha \pm \theta) = \cos(\alpha)\cos(\theta) \mp \sin(\alpha)\sin(\theta)$ have been used.
We now make a series expansion of the first factor in each term of Eq. (2.107):

$$e^{ik_1 r\cos(\alpha\mp\theta)} \approx e^{ik_1 r} e^{-\frac{1}{2}ik_1 r(\alpha\mp\theta)^2} . \tag{2.108}$$

For large values of $k_\rho \rho$, the parts of the integral where Eq. (2.108) is oscillating fast with α will vanish. The only parts that will remain is where $\alpha \approx \theta$ and $\alpha + \theta = \pi$. If we start by considering the case when $0 \leq \theta < \pi/2$, the integral reduces to

$$\overleftrightarrow{\mathbf{G}}^{(i,ff)}_{\phi\phi} \approx \frac{ie^{ik_1 r}}{8\pi}\sqrt{\frac{2}{\pi k_1 r\sin^2\theta}}r^{(s)}(k_\rho)k_\rho e^{ik_{z_1}z'}e^{-ik_\rho \mathbf{r}'\cdot\hat{\boldsymbol{\rho}}}e^{-\pi/4}\int_{\alpha=0}^{\pi/2} e^{-\frac{i}{2}k_1 r(\alpha-\theta)^2}\,d\alpha\,. \tag{2.109}$$

By extending the integration limits to go from $-\infty$ to $+\infty$, the integral can be evaluated using

$$\int_{-\infty}^{+\infty} e^{-ax^2}\,dx = \sqrt{\pi/a}\,, \tag{2.110}$$

which leads to the following expression:

$$\overleftrightarrow{\mathbf{G}}^{(i,ff)}_{\phi\phi} \approx \frac{ie^{ik_1 r}}{8\pi}\sqrt{\frac{2}{\pi k_1 r\sin^2\theta}}r^{(s)}(k_\rho)k_\rho e^{ik_{z_1}z'}e^{-ik_\rho \mathbf{r}'\cdot\hat{\boldsymbol{\rho}}}e^{-\pi/4}\sqrt{\frac{2\pi}{ik_1 r}} \tag{2.111}$$

$$= \frac{e^{ik_1 r}}{4\pi r}r^{(s)}(k_\rho)e^{ik_{z_1}z'}e^{-ik_\rho \mathbf{r}'\cdot\hat{\boldsymbol{\rho}}}\,, \tag{2.112}$$

where $e^{-i\pi/4}\sqrt{-i} = -i$ have been used. The far-field expressions for the other terms in Eq. (2.92) can be obtained by the same approach, and are given by

$$\overleftrightarrow{\mathbf{G}}^{(i,ff)}_{\rho\rho} \approx \frac{e^{ik_1 r}}{4\pi r}r^{(p)}(k_\rho)e^{ik_{z_1}z'}e^{-ik_\rho \mathbf{r}'\cdot\hat{\boldsymbol{\rho}}}\frac{k_{z_1}^2}{k_1^2}\,, \tag{2.113}$$

$$\overleftrightarrow{\mathbf{G}}^{(i,ff)}_{zz} \approx \frac{e^{ik_1 r}}{4\pi r}r^{(p)}(k_\rho)e^{ik_{z_1}z'}e^{-ik_\rho \mathbf{r}'\cdot\hat{\boldsymbol{\rho}}}\frac{k_\rho^2}{k_1^2}\,, \tag{2.114}$$

$$\overleftrightarrow{\mathbf{G}}^{(i,ff)}_{\rho z/z\rho} \approx \pm\frac{e^{ik_1 r}}{4\pi r}r^{(p)}(k_\rho)e^{ik_{z_1}z'}e^{-ik_\rho \mathbf{r}'\cdot\hat{\boldsymbol{\rho}}}\frac{k_\rho k_{z_1}}{k_1^2}\,, \tag{2.115}$$

where the $\pm$ in Eq. (2.115) indicate $+$ for the $\hat{\boldsymbol{\rho}}\hat{\mathbf{z}}$-component, and $-$ for $\hat{\mathbf{z}}\hat{\boldsymbol{\rho}}$. By using the coordinate transformations given by

$$\hat{\boldsymbol{\rho}} = \sin\theta\,\hat{\mathbf{r}} + \cos\theta\,\hat{\boldsymbol{\theta}}\,, \tag{2.116a}$$

$$\hat{\boldsymbol{\phi}} = \hat{\boldsymbol{\phi}}\,, \tag{2.116b}$$

$$\hat{\mathbf{z}} = \cos\theta\,\hat{\mathbf{r}} - \sin\theta\hat{\boldsymbol{\theta}}\,, \tag{2.116c}$$

one can obtain the indirect far-field Green's tensor given by

$$\overleftrightarrow{\mathbf{G}}^{(i,ff)}(\mathbf{r},\mathbf{r}') = \frac{e^{ik_1 r}}{4\pi r} e^{-ik_\rho \mathbf{r}'\cdot\hat{\boldsymbol{\rho}}} e^{ik_{z_1} z'} \Big[r^{(s)}(k_\rho)\hat{\boldsymbol{\phi}}\hat{\boldsymbol{\phi}} \\ - r^{(p)}(k_\rho)\,\hat{\boldsymbol{\theta}} \left(\hat{\mathbf{z}}\,\frac{k_\rho}{k_1} + \hat{\boldsymbol{\rho}}\,\frac{k_{z_1}}{k_1} \right) \Big] . \tag{2.117}$$

The transmitted far-field Green's tensor can be obtained by a similar approach, yielding

$$\overleftrightarrow{\mathbf{G}}^{(t,ff)}(\mathbf{r},\mathbf{r}') = \frac{e^{ik_2 r}}{4\pi r} e^{ik_{z_1} z'} e^{-ik_\rho \mathbf{r}'\cdot\hat{\boldsymbol{\rho}}} \frac{k_{z_2}}{k_{z_1}} \Big[t^{(s)}(k_\rho)\hat{\boldsymbol{\phi}}\hat{\boldsymbol{\phi}} \\ + t^{(p)}(k_\rho)\frac{\varepsilon_1}{\varepsilon_2} \left\{ \hat{\mathbf{z}}\hat{\mathbf{z}}\,\frac{k_\rho^2}{k_1^2} + \hat{\boldsymbol{\rho}}\hat{\boldsymbol{\rho}}\,\frac{k_{z_1}k_{z_2}}{k_1^2} + \left(\hat{\mathbf{z}}\hat{\boldsymbol{\rho}} + \hat{\boldsymbol{\rho}}\hat{\mathbf{z}}\frac{k_{z_2}}{k_{z_1}} \right) \frac{k_\rho k_{z_1}}{k_1^2} \right\} \Big] . \tag{2.118}$$

The last term that is needed in order to calculate the far-field radiation patterns is the expression for the far-field direct Green's tensor. In a Cartesian coordinate system $\overleftrightarrow{\mathbf{G}}^{(d)}(\mathbf{r},\mathbf{r}')$ can be written as

$$\overleftrightarrow{\mathbf{G}}^{(d)}(\mathbf{r},\mathbf{r}') = \left[\overleftrightarrow{\mathbf{I}} \left\{ 1 + \frac{i}{kR} - \frac{1}{(kR)^2} \right\} - \frac{\mathbf{RR}}{R^2} \left\{ 1 + \frac{3i}{kR} - \frac{3}{k^2R^2} \right\} \right] \frac{e^{ik_1|\mathbf{r}-\mathbf{r}'|}}{4\pi|\mathbf{r}-\mathbf{r}'|} , \tag{2.119}$$

where $R = |\mathbf{R}| = |\mathbf{r}-\mathbf{r}'|$, and $\mathbf{RR}$ denotes the outer product between $\mathbf{R}$ and itself [5]. In the far-field, when $R \gg \lambda$, the only terms that survives are

$$\begin{aligned} \overleftrightarrow{\mathbf{G}}^{(d,ff)}(\mathbf{r},\mathbf{r}') &= \left[\overleftrightarrow{\mathbf{I}} - \frac{\mathbf{RR}}{R^2} \right] \frac{e^{ik_1|\mathbf{r}-\mathbf{r}'|}}{4\pi|\mathbf{r}-\mathbf{r}'|} \\ &= \left[\overleftrightarrow{\mathbf{I}} - \hat{\mathbf{r}}\hat{\mathbf{r}} \right] \frac{e^{ik_1|\mathbf{r}-\mathbf{r}'|}}{4\pi|\mathbf{r}-\mathbf{r}'|} \\ &= \left[\hat{\boldsymbol{\theta}}\hat{\boldsymbol{\theta}} + \hat{\boldsymbol{\phi}}\hat{\boldsymbol{\phi}} \right] \frac{e^{ik_1 r}}{4\pi r} e^{-ik_1\hat{\mathbf{r}}\cdot\mathbf{r}'} . \end{aligned} \tag{2.120}$$

The far-field radiation pattern can now be obtained by using $\overleftrightarrow{\mathbf{G}}^{(d,ff)}$ and $\overleftrightarrow{\mathbf{G}}^{(i,ff)}$ for medium 1, and $\overleftrightarrow{\mathbf{G}}^{(t,ff)}$ for medium 2.

2.4 METHOD OF MOMENTS

In this section the concept of the method of moment is presented. This is based on [11] and [1].

The *method of moments* (MoM) is a numerical technique for solving a linear operator equation by converting it into a matrix equation. This method was first

applied to electromagnetic field problems by Harrington in 1968 [12], and has since been used to find numerical solutions to various scattering and radiation problems. The general technique is as follows.
Consider the equation given by

$$\mathcal{L}(f) = g\,, \tag{2.121}$$

where $\mathcal{L}$ is a known linear operator, g is a known excitation function, and f is an unknown response function. The unknown function f is approximated by a finite series of *basis functions* f_n as

$$f \approx \sum_{n}^{N} \alpha_n f_n\,, \tag{2.122}$$

where α_n are unknown constants. Substituting Eq. (2.122) into Eq. (2.121), and using the linearity of the operator yields

$$\sum_{n}^{N} \alpha_n \mathcal{L}(f_n) \approx g\,. \tag{2.123}$$

Next, a set of *testing functions* w_m are defined, and the inner product between each w_m and Eq. (2.123) are taken,

$$\sum_{n}^{N} \alpha_n \langle w_m, \mathcal{L}(f_n)\rangle = \langle w_m, g\rangle\,, \quad m = 1, 2, ..., N\,, \tag{2.124}$$

where the inner product is defined by

$$\langle w_m, f_n\rangle = \int_{w_m} w_m(\mathbf{r}) \cdot \int_{f_n} f_n(\mathbf{r}')\, d\mathbf{r}' d\mathbf{r}\,. \tag{2.125}$$

Equation (2.124) can be formulated as a matrix equation in the form of

$$\bar{\bar{Z}}\mathbf{a} = \mathbf{b}\,, \tag{2.126}$$

where

$$\bar{\bar{Z}} = \begin{bmatrix} \langle w_1, \mathcal{L}(f_1)\rangle & \langle w_1, \mathcal{L}(f_2)\rangle & \cdots & \langle w_1, \mathcal{L}(f_N)\rangle \\ \langle w_2, \mathcal{L}(f_1)\rangle & \langle w_2, \mathcal{L}(f_2)\rangle & \cdots & \langle w_2, \mathcal{L}(f_N)\rangle \\ \vdots & \vdots & \ddots & \vdots \\ \langle w_N, \mathcal{L}(f_1)\rangle & \langle w_N, \mathcal{L}(f_2)\rangle & \cdots & \langle w_N, \mathcal{L}(f_N)\rangle \end{bmatrix},$$

$$\mathbf{a} = \begin{bmatrix} \alpha_1 \\ \alpha_2 \\ \vdots \\ \alpha_N \end{bmatrix}, \quad \mathbf{b} = \begin{bmatrix} \langle w_1, g\rangle \\ \langle w_2, g\rangle \\ \vdots \\ \langle w_N, g\rangle \end{bmatrix}.$$

If the matrix $\bar{\bar{Z}}$ is invertible, the unknown coefficients α_n can be calculated by solving Eq. (2.126) to obtain

$$\mathbf{a} = \bar{\bar{Z}}^{-1}\mathbf{b}\,. \tag{2.127}$$

By substituting Eq. (2.127) into (2.122) an approximated solution for f can be found.
When MoM is applied to the electromagnetic problems discussed in this thesis, the known excitation function g corresponds to an incident electromagnetic field, f is the induced current, and $\mathcal{L}(f)$ is the electromagnetic field due to f. The $\bar{\bar{Z}}$ matrix is also known as the impedance matrix.
The choice of basis and testing functions will affect the accuracy of the solution to Eq. (2.122), as well as how efficient the solution is, since the complexity of the functions will increase computation time when evaluating the inner products. Though simple basis functions may require a large N in order to obtain an accurate solution, the inner products may be computationally easier to handle than more complex functions. There are no specific guidelines for choosing which basis functions to use, but one of the most crucial characteristics they must posses is to represent the expected behaviour of the unknown function as exact as possible. The basis functions should however not have smoother properties than the unknown function [13]. Choosing the testing functions such that $f_n = w_m$ is known as the Galerkin's method, and will result in a symmetric $\bar{\bar{Z}}$ matrix, due to the symmetry of $\langle .,. \rangle$. This can be exploited to reduce computation time when implementing a MoM code, since the lower diagonal elements of $\bar{\bar{Z}}$ are equal to the upper diagonal elements, however if the integrals are solved numerically, e.g. by Gaussian quadrature, the approximations may destroy the symmetry of the impedance matrix.

2.4.1 *RWG Basis Functions*

The choice of basis functions is very tricky, and it all comes down to trying to get the solution to converge. As mentioned, simple basis functions may be relatively easy to implement, but could require a large number of N in order to converge, whereas more advanced basis functions will reduce the number of unknowns in the matrix equation but at the cost of more complicated code that could take longer to run. One of the most commonly used basis functions for triangular tessellations are the *Rao-Wilton-Glisson* (RWG) basis functions, proposed in 1982 [14].
The RWG basis functions is defined by

$$\mathbf{f}_n(\mathbf{r}) = \begin{cases} \dfrac{\ell_n}{2A_n^+}\boldsymbol{\varrho}_n^+(\mathbf{r}) & \text{for } \mathbf{r} \in T_n^+ \\ \dfrac{\ell_n}{2A_n^-}\boldsymbol{\varrho}_n^-(\mathbf{r}) & \text{for } \mathbf{r} \in T_n^- \\ 0 & \text{otherwise}\,, \end{cases} \tag{2.128}$$

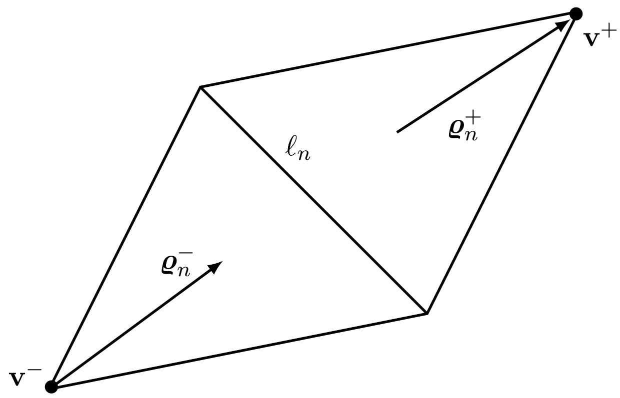

FIGURE 2.2 – The RWG basis function are assigned to an edge shared by two adjacent triangles. The definition ensures that no current pile-up on edges.

where T_n^+ and T_n^- are triangles sharing edge n, ℓ_n is the length of the edge, A_n^+ is the area of T_n^+, and the vectors $\boldsymbol{\varrho}_n^+(\mathbf{r})$, $\boldsymbol{\varrho}_n^-(\mathbf{r})$ are given by

$$\boldsymbol{\varrho}_n^+(\mathbf{r}) = \mathbf{v}^+ - \mathbf{r}\,, \quad \mathbf{r} \in T_n^+ \tag{2.129a}$$

$$\boldsymbol{\varrho}_n^-(\mathbf{r}) = \mathbf{r} - \mathbf{v}^-\,, \quad \mathbf{r} \in T_n^-\,, \tag{2.129b}$$

where the vertices $\mathbf{v}^+, \mathbf{v}^-$ are as shown in Figure 2.2. The RWG basis functions are only assigned to interior edges of a mesh, but for a closed surface all edges will be assigned a function, meaning each triangle will be assigned three RWG functions. Not only are the surface current $\mathbf{J}$ approximated by the basis function, but the basis functions also approximates the original surface [15]. It is therefore important to have a good tessellation of the surface, and ensure a reasonable triangle aspect ratio.

2.5 ARBITRARY THREE-DIMENSIONAL ANTENNA

For simple structures, e.g. closed-end cylinders or spheres, it is possible to define the geometry in MATLAB, but for more complicated structures, it is more convenient to use *computer aided design* (CAD) software to define the structure. The 3D surface is divided into a number of connected patches. Typically, triangular-or sometimes quadrilateral patches are used to make a polygon mesh of the surface. The patches can be flat, or curvilinear.
In Subsection 2.1.1 we found an integral equation for the radiation of electric fields due to surface currents, and in Subsection 2.1.2 we considered the scattering of a PEC, which led to the EFIE that relates the tangential component of the scattered field at the surface to the incident field:

$$-\frac{i}{\omega\mu}\hat{\mathbf{n}}(\mathbf{r}) \times \mathbf{E}_i(\mathbf{r}) = \hat{\mathbf{n}} \times \iint_S \overleftrightarrow{\mathbf{G}}(\mathbf{r}, \mathbf{r}') \cdot \mathbf{J}(\mathbf{r}')\, d\mathbf{r}'\,.$$

We will now apply the MoM to the scattering problem. The unknown current $\mathbf{J}(\mathbf{r}')$ is expanded into a finite sum of weighted basis functions:

$$\mathbf{J}(\mathbf{r}') = \sum_{n=1}^{N} \alpha_n \mathbf{f}_n(\mathbf{r}')\,. \tag{2.130}$$

Substituting Eq. (2.130) into the EFIE yields

$$-\frac{i}{\omega\mu}\hat{\mathbf{n}} \times \mathbf{E}_i(\mathbf{r}) = \left[\overleftrightarrow{\mathbf{I}} + \frac{1}{k^2}\nabla\nabla\cdot\right] \int_{\mathbf{f}_n} g(\mathbf{r},\mathbf{r}') \sum_{n=1}^{N} \alpha_n \mathbf{f}_n(\mathbf{r}')\, d\mathbf{r}'\,, \tag{2.131}$$

where $\mathbf{f}_n(\mathbf{r}')$ is everywhere tangential to the surface. By applying the testing functions $\mathbf{f}_m(\mathbf{r})$ we obtain $\bar{\bar{Z}}$-matrix elements given by

$$\begin{aligned} Z_{m,n} = &\int_{\mathbf{f}_m} \mathbf{f}_m(\mathbf{r}) \cdot \int_{\mathbf{f}_n} g(\mathbf{r},\mathbf{r}')\mathbf{f}_n(\mathbf{r}')\, d\mathbf{r}' d\mathbf{r} \\ &+ \frac{1}{k^2}\int_{\mathbf{f}_m} \mathbf{f}_m(\mathbf{r}) \cdot \left[\nabla\nabla \cdot \int_{\mathbf{f}_n} g(\mathbf{r},\mathbf{r}')\mathbf{f}_n(\mathbf{r}')\, d\mathbf{r}'\right] d\mathbf{r}\,, \end{aligned} \tag{2.132}$$

and excitation elements b_m given by

$$b_m = -\frac{i}{\omega\mu}\int_{\mathbf{f}_m} \mathbf{f}_m(\mathbf{r}) \cdot \mathbf{E}_\mathbf{i}(\mathbf{r})\, d\mathbf{r}\,. \tag{2.133}$$

Let us consider the second term in Eq. (2.132), which can be rewritten:

$$\begin{aligned} \mathcal{I}_2(\mathbf{r}) &= \int \mathbf{f}_m(\mathbf{r}) \cdot \left[\nabla\nabla \cdot \int \mathbf{f}_n(\mathbf{r}')g(\mathbf{r},\mathbf{r}')\, d\mathbf{r}'\right] d\mathbf{r} \\ &= \int \mathbf{f}_m(\mathbf{r}) \cdot \left[\nabla \int g(\mathbf{r},\mathbf{r}')\nabla' \cdot \mathbf{f}_n(\mathbf{r}')\, d\mathbf{r}'\right] d\mathbf{r} \\ &= \int \mathbf{f}_m(\mathbf{r}) \cdot \nabla\mathcal{H}(\mathbf{r})\, d\mathbf{r}\,, \end{aligned} \tag{2.134}$$

where $\mathcal{H}(\mathbf{r}) = \int g(\mathbf{r},\mathbf{r}')\nabla' \cdot \mathbf{f}_n(\mathbf{r}')d\mathbf{r}'$. A detailed proof of the operation used in the bracket term is derived in Appendix B. By using the vector identity given by Eq. (B.3), the integrand in Eq. (2.134) can be reformulated, and allows for the equation to be expressed as

$$\mathcal{I}_2(\mathbf{r}) = \int \nabla \cdot \Big[\mathbf{f}_m(\mathbf{r})\mathcal{H}(\mathbf{r})\Big] - \Big[\nabla \cdot \mathbf{f}_m(\mathbf{r})\Big]\mathcal{H}(\mathbf{r})\, d\mathbf{r}\,, \tag{2.135}$$

where we can apply Gauss' divergence theorem to the first term, and make the bounding surface large enough to make the integral vanish, leaving only the second term:

$$\begin{aligned} \mathcal{I}_2(\mathbf{r}) &= -\int \Big[\nabla \cdot \mathbf{f}_m(\mathbf{r})\Big]\mathcal{H}(\mathbf{r})\, d\mathbf{r} \\ &= -\int \nabla \cdot \mathbf{f}_m(\mathbf{r}) \int g(\mathbf{r},\mathbf{r}')\nabla' \cdot \mathbf{f}_n(\mathbf{r}')\, d\mathbf{r}'\, d\mathbf{r}\,. \end{aligned} \tag{2.136}$$

Let us now consider the RWG functions as our choice of basis functions. For an arbitrary 3D antenna structure with a triangular mesh, the impedance matrix elements can thus be obtained from

$$Z_{m,n} = \iint\limits_{\mathbf{f}_m} \iint\limits_{\mathbf{f}_n} \left\{ \mathbf{f}_m(\mathbf{r}) \cdot \mathbf{f}_n(\mathbf{r}') - \frac{1}{k^2} \Big[\nabla \cdot \mathbf{f}_m(\mathbf{r}) \Big] \Big[\nabla' \cdot \mathbf{f}_n(\mathbf{r}') \Big] \right\} \frac{e^{ikr}}{4\pi r} \, d\mathbf{r}' d\mathbf{r} \,, \quad (2.137)$$

where the divergence of the RWG-basis functions are given by

$$\nabla \cdot \mathbf{f}_n(\mathbf{r}) = \begin{cases} -\dfrac{\ell_n}{A_n^+} & \text{for } \mathbf{r} \in T_n^+ \\ \dfrac{\ell_n}{A_n^-} & \text{for } \mathbf{r} \in T_n^- \\ 0 & \text{otherwise} \,. \end{cases} \quad (2.138)$$

The integrals in Eq. (2.137) are over two RWG functions, which span two triangles each. Since the dipole surface is closed, each triangle supports three RWG basis functions, and the integration over a source and observation triangle contributes to nine matrix elements. It is therefore more efficient to perform outer loops over source and test triangles and inner loops over basis functions, and add the results to the appropriate matrix elements.
For a single source and test triangle, Eq. (2.137) are given by

$$\mathcal{I} = \frac{L_m L_n}{A_m A_n} \iint\limits_{T_m} \iint\limits_{T_n} \left\{ \frac{1}{4} \boldsymbol{\varrho}_m^{\pm}(\mathbf{r}) \cdot \boldsymbol{\varrho}_n^{\pm}(\mathbf{r}') \pm \frac{1}{k^2} \right\} \frac{e^{ikr}}{4\pi r} \, d\mathbf{r}' d\mathbf{r} \,. \quad (2.139)$$

For non-near terms, one can generally use numerical methods, such as the Gaussian quadrature rule, to approximate the integrals. The Gaussian quadrature rule is a method of approximating a definite integral of a function by a weighted sum of the function evaluated at specific points within the integration domain. For M evaluation points, the integral can be approximated by

$$\mathcal{I} \simeq \frac{L_m L_n}{4\pi} \sum_{p=1}^{M} \sum_{q=1}^{M} w_p w_q \left\{ \frac{1}{4} \boldsymbol{\varrho}_m^{\pm}(\mathbf{r}_p) \cdot \boldsymbol{\varrho}_n^{\pm}(\mathbf{r}'_q) \pm \frac{1}{k^2} \right\} \frac{e^{ikR_{pq}}}{R_{pq}} \,, \quad (2.140)$$

where w_i is the weight of the i'te point, and

$$R_{pq} = \sqrt{(x_p - x_q)^2 + (y_p - y_q)^2 + (z_p - z_q)^2} \,. \quad (2.141)$$

For self-coupling terms, i.e. when triangles overlap, a common method for handling the singularities are the *singularity extraction*, which uses the following expression:

$$\frac{e^{ikr}}{r} = \left[\frac{e^{ikr}}{r} - \frac{1}{r} \right] + \frac{1}{r} \,. \quad (2.142)$$

The first term on the right-hand side of Eq. (2.142) can be used in directly Eq. (2.140) since it is well behaved for all values of r in this limit:

$$\lim_{\mathbf{r}\to 0}\left[\frac{e^{ikr}}{r}-\frac{1}{r}\right]=ik\,. \tag{2.143}$$

Therefore, only the $1/r$ term must be handled with care when performing the integration:

$$\mathcal{I}_{1/r}=\frac{L_mL_n}{A_mA_n}\iint\limits_{T_m}\iint\limits_{T_n}\left\{\frac{1}{4}\boldsymbol{\varrho}_m^{\pm}(\mathbf{r})\cdot\boldsymbol{\varrho}_n^{\pm}(\mathbf{r}')\pm\frac{1}{k^2}\right\}\frac{1}{r}\,d\mathbf{r}'d\mathbf{r}\,. \tag{2.144}$$

When T_m and T_n overlap, the inner and outer integration in Eq. (2.144) can be calculated analytically. The basis function vector $\boldsymbol{\varrho}_{m,n}$ are first converted into simplex coordinates. For the basis function $\boldsymbol{\varrho}^-(\mathbf{r})$ on T^-, the simplex coordinate is given by

$$\boldsymbol{\varrho}(\mathbf{r})=(1-\lambda_1-\lambda_2)\,\mathbf{v}_1+\lambda_1\mathbf{v}_2+\lambda_2\mathbf{v}_3-\mathbf{v}_{m,n}\,, \tag{2.145}$$

where $\mathbf{v}_1,\mathbf{v}_2$ and $\mathbf{v}_3$ are triangle vertices, $\mathbf{v}_{m,n}$ are the vertex opposite edge on the triangle, and λ_i are the simplex coordinates. So for $\boldsymbol{\varrho}^-(\mathbf{r})$ on T^-, the integrals over the first term in Eq. (2.144) is on the form of

$$\begin{aligned}\mathcal{I}_{1/r,1}=\iint_{T_m}\iint_{T_n}&\Big\{(1-\lambda_1-\lambda_2)\mathbf{v}_1+\lambda_1\mathbf{v}_2+\lambda_2\mathbf{v}_3-\mathbf{v}_m\Big\}\\&\cdot\Big\{(1-\lambda_1-\lambda_2)\mathbf{v}_1+\lambda_1\mathbf{v}_2+\lambda_2\mathbf{v}_3-\mathbf{v}_n\Big\}\frac{1}{r}\,d\mathbf{r}'d\mathbf{r}\,.\end{aligned} \tag{2.146}$$

By multiplying the terms in the above results in a set of integrals of the form

$$C\iint_{T_m}\iint_{T_n}\lambda_i\lambda_j'\frac{1}{|\mathbf{r}-\mathbf{r}'|}\,d\mathbf{r}'d\mathbf{r}\,. \tag{2.147}$$

Eibert and Hansen in [16, 17] have evaluated these integrals analytically. By using the edge lengths of the considered triangles defined by

$$l_1=|\mathbf{v}_2-\mathbf{v}_3|\,, \tag{2.148a}$$
$$l_2=|\mathbf{v}_3-\mathbf{v}_1|\,, \tag{2.148b}$$
$$l_3=|\mathbf{v}_1-\mathbf{v}_2|\,, \tag{2.148c}$$

the results are given as

$$\frac{1}{4A^2}\iint_{T_m}\iint_{T_n}\frac{1}{|\mathbf{r}-\mathbf{r}'|}\,d\mathbf{r}'d\mathbf{r}=\frac{1}{3l_1}\ln_1+\frac{1}{3l_2}\ln_2+\frac{1}{3l_3}\ln_3\,, \tag{2.149}$$

$$\begin{aligned}\frac{1}{4A^2}\iint_{T_m}\iint_{T_n}\lambda_1'\lambda_1\frac{1}{|\mathbf{r}-\mathbf{r}'|}\,d\mathbf{r}'d\mathbf{r}&=\frac{1}{20l_1}\ln_1+\frac{l_1^2+5l_2^2-l_3^2}{120l_2^3}\ln_2\\&+\frac{l_1^2-l_2^2+5l_3^2}{120l_3^3}\ln_3+\frac{l_3-l_1}{60l_2^2}+\frac{l_2-l_1}{60l_3^2}\,,\end{aligned} \tag{2.150}$$

$$\begin{aligned}\frac{1}{4A^2}\iint_{T_m}\iint_{T_n}\lambda_2'\lambda_1\frac{1}{|\mathbf{r}-\mathbf{r}'|}\,d\mathbf{r}'d\mathbf{r}&=\frac{3l_1^2+l_2^2-l_3^2}{80l_1^3}\ln_1+\frac{l_1^2+3l_2^2-l_3^2}{80l_2^3}\ln_2\\&+\frac{1}{40l_3}\ln_3+\frac{l_3-l_2}{40l_1^2}+\frac{l_3-l_1}{40l_2^2}\,,\end{aligned} \tag{2.151}$$

$$\begin{aligned}\frac{1}{4A^2}\iint_{T_m}\iint_{T_n}\lambda_1'\frac{1}{|\mathbf{r}-\mathbf{r}'|}\,d\mathbf{r}'d\mathbf{r}&=\frac{1}{8l_1}\ln_1+\frac{l_1^2+5l_2^2-l_3^2}{48l_2^3}\ln_2\\&+\frac{l_1^2-l_2^2+5l_3^2}{48l_3^3}\ln_3+\frac{l_3-l_1}{24l_2^2}+\frac{l_2-l_1}{24l_3^2}\,,\end{aligned} \tag{2.152}$$

where

$$\ln_1=\log\left[\frac{(l_1^2+l_2^2)-l_3^2}{l_2^2-(l_3-l_1)^2}\right]\,,\quad \ln_2=\log\left[\frac{(l_2+l_3)^2-l_1^2}{l_3^2-(l_1-l_2)^2}\right]\,,$$

$$\ln_3=\log\left[\frac{(l_3+l_1)^2-l_2^2}{l_1^2-(l_2-l_3)^2}\right]\,.$$

The remaining integrals involving the integrand in Eq. (2.146) can be obtained by permutation of the vertex indices [16]. These analytic expressions for the self-coupling terms are fast to calculate, but the preliminary mathematical work is extensive. Another method, which is less accurate, is to use numerical integration on the self-coupling terms as well. If the source points do no coincide with the testing points, the quadrature method can be used to approximate all integrals. A simple approach would be to divide the source triangles into nine sub-triangles and perform a nine-point quadrature on the source integrals, and only use a one-point quadrature on the testing integrals. A similar method was tested by Makarov in [18]: the nine-point quadrature was applied to all non-near terms, whilst the self-coupling terms were evaluated using the analytic expression given by Eq. (2.149). The basis functions $\boldsymbol{\varrho}(\mathbf{r})$ were replaced by their values at the center of the triangle, thereby omitting the need for the rest of the analytic expressions given by [16]. The results of this method were compared to when the nine-point quadrature were used for self-coupling terms as well. According to Makarov, both approaches produced very similar results, and notes the calculations produced a deviance in the surface current magnitudes of less that 1%.

CHAPTER 3

Implementation

In this chapter the implementation will be presented, first the structure of the script will be reviewed, then select methods of interest will be further examined. This will be done by presenting considerations for how the code is structured, how the equations are implemented and what inputs the script accepts.

3.1 Script Structure

The script is split into two parts, the “MoMScript” which is the executed part and the “ArbitraryAntenna” class, which holds methods used for the computations. This split is used to ease readability and increases modularity of the code.

3.1.1 *Import of STL File*

This section in the “MainScript” loads the STL file specified by the string. It returns an STL object that holds a p-matrix of points and a t-matrix of triangle points. The p-matrix holds x, y, z-coordinates as the first, second and third column respectively and each row constitutes a point. The t-matrix consists of each corner of a triangle as columns with each row constituting a triangle. The corners are numbered and the number corresponds to an index in the p-matrix. So for example a row from the t-matrix consisting of $(1, 2, 3)$ means that the coordinates to the corners are found in the p-matrix first, second and third row. The STL file reader used in this code is the “STL File Reader” [19]. This STL reader is limited to STL files saved in binary format, and an error will be produced if an attempt is made at loading a STL file saved in ASCII format. The STL reader function could be replaced with any equivalent or even loading the p-

and t-matrices directly from a saved file, the only restriction is that the dimensions must match what is described above.

3.1.2 *Remove Duplicate Points*

Due to the way the STL files are created in Fusion360, there are some points that overlap and appear more than once. In order to save calculation time these points are identified and pruned.
This is done by first identifying points that share coordinates and saving their indices. The lowest of these indices are used as replacement in the t-matrix, for instance if the points 1, 27, 48 and 537 were the same point the occurrences of 27, 48 and 537 would be set to 1 in the t-matrix. Lastly the redundant points are removed from the p-matrix and the p-matrix are updated with the new indices.

3.1.3 *Duplicate Antennas*

This thesis have used the script to examine dipole antenna, however it was also of interest to examine how multiple dipole antenna interact with each other. This is an option within the script, however no method can do it automatically, therefore an outline of the procedure will be given here. Once the p-and t matrices have been created these can be manipulated in order to create different structures, the methods are a result of the p matrix consisting of coordinates and the t matrix the indices of these coordinates. When the STL file is loaded the coordinates will correspond to the placement in the coordinate system that the antenna had in Fusion360, in this thesis this corresponds to the center of the antenna at the origin, and as such it can be translated in any direction. In order to displace an antenna along the z-axis one simply expresses the new z-coordinates as the old ones plus the wanted displacement i.e. $p(:,3) = p(:,3) + 2$ would displace the antenna 2 meters in the positive z-direction. This can also be done for displacements in a negative direction writing $p(:,3) = p(:,3) - 2$ for the same antenna would return it to its original position. In addition to moving the antenna it can also be scaled in its dimensions $p = 2 \cdot p$ would result in an antenna with twice the size as the original, this scaling can also be applied to single dimensions, if the length of the antenna is in the y-direction $p(:,2) = 2 \cdot p(:,2)$ gives an antenna with twice the length but without changing the diameter, if the wavelength is scaled with the length increase this effectively halves the diameter. The translation of antenna can also be used to create different structures by assigned the translated structure to a new p-matrix and then concatenating them i.e. duplicating p into $p1$ and $p2$ followed by assignments

$$
\begin{aligned}
p1(:,3) &= p1(:,3) + 0.1\,, \\
p2(:,3) &= p2(:,3) - 0.1\,, \\
p &= [p1; p2]\,.
\end{aligned}
$$

Next, the t matrix also needs to be updated. This is done by assignment

$$t = [t1; t2 + length(p1); t3 + length(p1) + length(p2)] \,,$$

in order to extend this to more antenna the length of p should be added an additional time for each added antenna.
The approach outlined here uses the same initial mesh for all duplicated antennas, but it can also be done for different meshes, if $p1, p2$ and $p3$ are the p matrices from different STL files and $t1, t2$ and $t3$ are their corresponding t matrices then the combined p-matrix is

$$p = [p1; p2; p3] \,,$$

and the combined t-matrix is

$$t = [t1; t2 + length(p1); t3 + length(p1) + length(p2)] \,.$$

When combining multiple antenna in this way, the scaling method can also be applied. If one wishes to sale the entire system, it can be applied after the concatenation, however, one could also change the scaling of a single antenna before concatenation.

3.1.4 *Calculation of Antenna Dimensions*

Dimension calculation within the script is set to calculate for a dipole, but will attempt to calculate dimension for any imported structure. The length is found by determining the maximum value of the p-matrix and determining in which dimension it is a maximum. Then the minimum value in the same dimension is subtracted, thus giving the length denoted by L. The radius is determined by averaging the absolute of the minimum and maximum values in the two remaining dimensions. For the dipole antenna modeled in this thesis, this means
$L = max(y) - min(y)$ and
$radius = (|min(x)| + |min(z)| + |max(x)| + |max(z)|)/4$. The wavelength is set to $2L$, resulting in a half-wavelength antenna, as these are typically the most effective. The wavelength can however easily be changed to other values in order to examine alternate radiation patterns. The diameter is used to determine the minimum displacement needed for the silicon interface to avoid an overlap between the interface and the antenna.

3.1.5 *Additional Triangle Information*

In order to evaluate the RWG functions, some intermediate calculations are done for each triangle. Firstly, the area and the center point of each triangle is found: these are saved in $Area$ and $Center$, respectively. In order to calculate the Gaussian quadrature each triangle is split into sub-triangles: This is done by calculating the coordinates of the points located at 1/3 and 2/3 of the length on each edge in the original triangle. These points, the original corner points as well

as the center point, are used to create nine sub-triangles. The center points of these are saved in the matrix $SubTri$. The matrix $SubTri$ has the dimensions: $[Amountofsub - triangles, 3, amountoftriangles]$.
$SubTri(:,:,1)$ returns the center points of the sub-triangles contained in triangle 1. Additionally, the script contains the option to further increase the amount of sub-triangles by creating nine sub-triangles within each sub-triangle, thus resulting in a total of 81 sub-triangles per triangle. This effectively makes the 9-point numerical quadrature into an 81-point numerical quadrature, if this option is used. Since the triangles supplied by the STL file are plane triangles with the corner points placed on the surface, this method leads to a faceted surface with the center points placed slightly inside the antenna. In order to correct for this, the script contains a method for lifting the points in $Center$ and $SubTri$ to the actual surface of the antenna. This is done by separating the antenna into three sections: an upper sphere, a cylinder and a lower sphere. The upper and lower spheres use the center of the sphere as a baseline point, in order to determine the direction of the normal vector to a given point and replaces this point by $CenterOfSphere + NormalVector \cdot radius$. The cylinder part employs the same method, however the $CenterOfSphere$ is replaced by the center of the cylinder with the y-value equal to the point currently being lifted. The method determines if the point to be lifted is on a sphere or cylinder by checking its y-coordinate against a preset value. Therefore the lift method takes a bool, $Lift$, that determines if the points should actually be lifted, for non dipole antenna or dipole antenna that have been scaled this $Lift$ should be zero. The method however should still be called as it changes the dimensions of the $SubTri$ matrix to the ones mentions earlier, and this is the format the script expects to receive.

3.1.6 *Identifying Edges*

In order to determine which edges exist for a structure, and therefore which basis functions need to be defined, a connectivity list is created as described by [1]. This is done by looping over all points and determining which triangles they are a part of. Then the remaining point of the triangle are identified along with their indices, and only points with indices higher than the current iteration in the for-loop are of interest. This is done to avoid finding the same edge twice. The information is stored in a cell, which for a given edge, holds the index of the starting point, the index of the end point, as well as indices for the triangles that the edge is a part of. The starting point is equal to the index in the list, while the end point indices are held as an array in the first column of the list and the triangle indices are held as an array in the second column.
The connectivity list is used to create the *EdgeList* in order to ease accessibility to the information, as the *EdgeList* is stored as a matrix. Its indices corresponds to the numbering of edges, the first column holds the start point of the edge, second column holds the index of the end point. The third and fourth column hold the vertices needed to compute the basis functions, that is to say the vertices

opposite the edge. The third column holds the vertices used to compute $\boldsymbol{\varrho}^+$ and the fourth column the vertices used to compute $\boldsymbol{\varrho}^-$, the vertex with the lowest index is always assigned as the positive vertex.
The RWG basis functions are created in the same loop as the *EdgeList* is created. These are saved as function handles in the cell *Basis*. The row indices in *Basis* corresponds to the edge number, the first column holds the $\boldsymbol{\varrho}^+$ function handles, while the second column hold the $\boldsymbol{\varrho}^-$ function handles, these correspond to Eqs. (2.129). The remaining part of the basis functions are stored separately in the matrix *BasisLA* with the same row indexing: the first column holds $L/2A_p$, second column holds L and the third column holds $L/2A_m$. Here A_p and A_m corresponds to the *Area* of the plus and minus triangles respectively. The length is stored separately to reduce calculations when employing a numerical quadrature solution to the integrals of the MoM method, as the areas will cancel out. The function handles are evaluated in the center points of their respective triangles, and in the corresponding sub-triangles. These values are saved in *RhoP*, *RhoM*, *RhoP_* and *RhoM_*, where the underscore denotes that the values belong to sub-triangles center points.

3.1.7 *Options for Excitation of Antenna*

In order to determine the excitation vector, given by Eq. (2.133), one needs to calculate the incident field. In this script, the incident field is calculated in the center of each triangle on the antenna. Given that there are both plus and minus triangles the expression becomes [18]

$$b_m = \frac{L}{2}\Big[\mathbf{E}_i(\mathbf{r}_{c^+})\cdot\boldsymbol{\varrho}(\mathbf{r}_{c^+}) + \mathbf{E}_i(\mathbf{r}_{c^-})\cdot\boldsymbol{\varrho}(\mathbf{r}_{c^-})\Big]\,. \tag{3.1}$$

The script has three options for excitation of the antenna: a plane wave, a point source, and a voltage feed. A plane wave is expressed by

$$\mathbf{E}_i(\mathbf{r}) = \hat{\mathbf{x}}\, e^{i\mathbf{k}\cdot\mathbf{r}} + \hat{\mathbf{y}}\, e^{i\mathbf{k}\cdot\mathbf{r}} + \hat{\mathbf{z}}\, e^{i\mathbf{k}\cdot\mathbf{r}}\,, \tag{3.2}$$

in the script, where the polarization is in the $\hat{\mathbf{y}}$-direction and the other polarization directions are set to zero. In addition the wave is chosen to propagate along the $\hat{\mathbf{z}}$ direction, so the values of $\mathbf{r}$ are chosen as the triangles center points z-coordinates. Even though the wave is only polarized in the $\hat{\mathbf{y}}$-direction the field is still represented as a matrix with the $\hat{\mathbf{x}}, \hat{\mathbf{y}}$, and $\hat{\mathbf{z}}$-polarization as the first, second and third column, respectively. This configuration makes it easier to change the incident fields polarization, as the script expects it to passed in matrix form and has no special restrictions on the polarization or propagation direction. When the excitation source is a point source, the incident field is calculated at the center points of the triangles in the method *PointSource*, here the location of the point source and the polarization is passed as the last two arguments. The electric field strength can be calculated from [5]

$$\mathbf{E}_i(\mathbf{r}) = \omega^2\mu\overleftrightarrow{\mathbf{G}}(\mathbf{r},\mathbf{r}')\cdot\mathbf{p}\,. \tag{3.3}$$

The most common configuration used for the point source is placing it an antenna length from the antenna in the $\hat{\mathbf{z}}$-direction and having it be polarized in the $\hat{\mathbf{y}}$-direction.
The third alternative for excitation is a voltage feed, this method is outlined in [18] for a strip. When employed for a strip one of the RWG edges is used as a driving edge, that is assumed to act as a voltage gap, this gives rise to an electric field within the gap given as

$$\mathbf{E} = \frac{V}{\Delta}\hat{\mathbf{y}} \,. \tag{3.4}$$

The gap is associated with an RWG edge so $\Delta \to 0$, as they do not have a physical width This in turn means that $E \to \infty$. Therefore, the field can be expressed as

$$\mathbf{E} = V\delta(y)\hat{\mathbf{y}} \,, \tag{3.5}$$

which means that the integral over the field is equal to the applied voltage. In terms of implementation, this means that an applied electric field is only present in the triangles which share the edge chosen as the feed edge. This results in a change of the excitation vector to

$$b_m = L\,V \,, \tag{3.6}$$

for the feed edge and 0 for the non-feed edge. In order to apply this method to a 3D dipole, the infinitesimal gap is chosen to be at $y = 0$, effective placing it in the middle of the antenna in the longitudinal direction. The voltage is then applied to all edges that coincide with this split. The excitation vector therefore is expanded to include all the edges that the voltage are applied to. This method for a voltage feed is not guaranteed to work for all meshes, as it requires perpendicular edges at $y = 0$. The feed position can however be changed, but in most cases a centered voltage feed in regard to the the antenna structure is wanted. If one wished to use a voltage feed in simulations, care should be taken to ensure that there exists edges that meet the given requirements. When multiple antennas are used in simulation the amount of antenna that receive a voltage feed can be changed, this is done through the variable $Yagi$, if it is true only the second antenna in the concatenated p-matrix is used as a feed antenna.

3.2 IMPLEMENTING THE METHOD OF MOMENTS

The script has implemented two equivalent ways of using the MoM. The difference lies in their approach: one is for-loop based and the other is vectorized. Both are included in Sections C.1 and C.2 in Appendix C, respectively. The difference between them will be outlined here, the for-loop based approach should easier to read and understand, however the difference in computational speed makes the vectorized method far superior. The MoM implementation is based on Eq.

TABLE 3.1 – Table with sample computation times for the impedance matrix for the two methods. N denotes the amount of basis functions with impedance matrix size being $N \times N$.

N	828	1053	1350
Loop-based [s]	50.37	87.11	129.65
Vectorized [s]	4.60	6.79	11.15

(2.140), and follow the quadrature schemes employed by [18], which are discussed in Section 2.4. Equation (2.140) expresses a single matrix element in the impedance matrix $\bar{\bar{Z}}$. The impedance matrix has dimensions $N \times N$ where N is the number of edges assigned an RWG basis function. In the implementation, Eq. (2.140) is split into multiple parts:

$$A^{\pm}_{mn} = \sum_{q=1}^{M} \frac{L_n}{8\pi w_q} \boldsymbol{\varrho}^{\pm}_n(\mathbf{r}'_q) \frac{e^{ikR_{pq}}}{R_{pq}} \,, \tag{3.7}$$

$$Dot^{\pm} = \frac{L_m}{w_p} A_{mn} \cdot \boldsymbol{\varrho}^{\pm}_m(\mathbf{r}_p) \,, \tag{3.8}$$

$$phi^{\pm} = \sum_{q=1}^{M} \frac{L_n}{4\pi k^2} \frac{e^{ikR_{pq}}}{R_{pq}} \,. \tag{3.9}$$

Given the quadrature approach, $w_q = 9$ and $w_p = 1$, which in the script are used by having $A^{\pm}_{mn}$ and $phi^{\pm}$ depend on distance to sub-triangles and $Dot^{\pm}$ depend on distance to the center of the triangle. Both the vectorized and the non-vectorized method use these sub calculations. The methods both loop over the m basis functions as an outer loop, the difference comes in how the n basis functions are treated. The non-vectorized method computes them in an inner for loop thus computing only one entry in the impedance matrix $Z_{m,n}$. The vectorized method calculates the interaction with all other basis functions for each m, thus calculating an entire row of the impedance matrix at a time, $Z_{m,N}$. In Table 3.1, the computation time for the two methods are presented. In addition to the faster computation times, the time scaling is also better, as the loop-based approach is $\mathcal{O}(n^2)$ while the vectorized is $\mathcal{O}(n)$.

3.2.1 *Current Calculation and Visualization*

The current is calculated for each triangle on the antenna, and for each triangle the current is assumed constant. From the expansion of the current into basis functions, Eq. (2.130), the current can be found from the coefficients determined by the MoM as well as the basis function. Given the way the RWG functions are distributed over the antenna, there are three RWG basis functions that will add to the current of a given triangle. In order to compute these values, a outer loop over triangles, and two inner loops over plus basis functions and minus basis functions

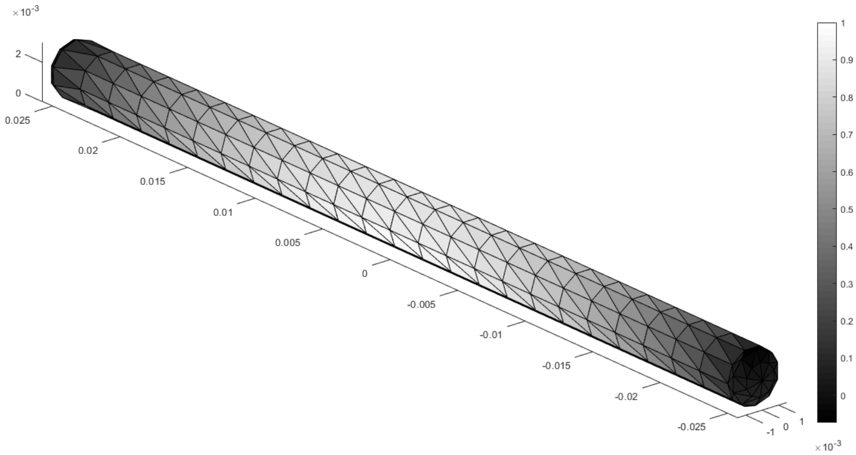

Figure 3.1 – 3D visualization of the surface current distribution of a half-wave dipole antenna. The antenna is scaled down by a factor of two in the longitudinal direction to increase visibility of the triangular mesh.

within the triangle, are performed. In order to visualize the current, two approaches are employed: one can plot the absolute value of the $\hat{\mathbf{y}}$-component of the current against the y-coordinate of the center of the triangle. This is adequate as the current in the other dimensions are essentially zero. The other computes the size of the current and normalizes it, then, by matching triangle corner points to the current, a 3D figure can be created. This figure represents the antenna structure, where each triangle receives a color relative to the value of the current. An example of this can be seen in Figure 3.1.

3.3 CALCULATION OF RADIATED FIELD

The script contains various ways of computing the radiated fields of antenna. These are based on the equations and thoughts presented in Section 2.2. The calculations of the scattered field are split into two different approaches: one type of method computes the radiation as a result of a current running through the antenna, which is based on 2.24. The second type of method is based on Eqs. (2.120), (2.117) and (2.118). This allows computation of the far-field radiation based on the angle of observation. These methods can be found in Sections 2.1.1 and C.4, respectively. The results of these methods are polar plots that illustrate the radiation patterns, these are useful tool in determining the directivity of an antenna or antenna configuration.

The first type of method computes the x-, y- and z-components of the radiated field in the xy-, xz- and zy-planes. In order to calculate the radiation in the three planes, an outer loop over these planes are employed. The method runs an inner loop over triangles, calculating the triangles contribution to the each component of the E-field in the current plane. The procedure for each plane is the same. The xy-plane is used here as an example for the computation method. First the x-distance and the y-distance are discretesized into the desired resolution. In the second loop three matrices are calculated: these contain the distance to each point in the area of interest from the center point of the triangle for the x-, y- and z-components respectively. The values in the R_x-matrix vary with rows, and the values in the R_y-matrix vary with columns. The R_z-matrix values are constant. These matrices are then used to compute the total distance to a point by $r = \sqrt{r_x^2 + r_y^2 + r_z^2}$, which in return is used to compute the parts of the Green's tensor split into

$$g = \frac{e^{ik\bar{\bar{r}}}}{4\pi\bar{\bar{r}}} ,$$

$$G1 = 1 + \frac{i}{k\bar{\bar{r}}} - \frac{1}{(k\bar{\bar{r}})^2} ,$$

and

$$G2 = 1 + \frac{3i}{k\bar{\bar{r}}} - \frac{3}{(k\bar{\bar{r}})^2} .$$

Note that the division occur element-wise. Next each direction of the Green's tensor are computed separately and used to compute a component of the radiated field. For the E-fields $\hat{\mathbf{x}}$-component in the xy-plane these are computed as

$$\bar{\bar{G}}_{xx} = \left(\bar{\bar{G}}1 - \frac{\bar{\bar{R}}_x\bar{\bar{R}}_x}{r^2}G2\right)\bar{\bar{g}} ,$$

$$\bar{\bar{G}}_{xy} = \left(-\frac{\bar{\bar{R}}_y\bar{\bar{R}}_y}{r^2}G2\right)\bar{\bar{g}} ,$$

$$\bar{\bar{G}}_{xz} = \left(-\frac{\bar{\bar{R}}_z\bar{\bar{R}}_z}{r^2}G2\right)\bar{\bar{g}} ,$$

and

$$\bar{\bar{E}}_{xyx} = i\omega\mu(\bar{\bar{G}}_{xx} \cdot \mathbf{J}_x + \bar{\bar{G}}_{xy} \cdot \mathbf{J}_y + \bar{\bar{G}}_{xz} \cdot \mathbf{J}_z) \cdot Area;$$

Note the missing term $\bar{\bar{G}}1$ in the $\bar{\bar{G}}_{xy}$ and $\bar{\bar{G}}_{xz}$ expressions, as the unit dyad does not contribute to this direction. These field components are then added to the previous total, in order to account for all triangles.
There are some considerations about which part the loop should run over. One can choose between computing the radiation for all points in the plane or for all triangles on the antenna, choosing which of these parameters should be used in the for loop should be done based on the amount of elements.

The second method type only calculates a vector that represents the angular far-field, this makes this method of computing the E-field much quicker given the less intensive calculations. These methods also employ a loop over triangles, however here it might be time beneficial to make a change of loop parameter as the resolution is also set at 200 steps. The method, as a baseline, computes the field for $\phi = \pi/2$ and letting $0 < \theta < 2\pi$, corresponding to the radiated field in the zy-plane. In the same approach as for the previous method each part of the Green's tensor is assigned to a variable, each corresponding to a direction. The radiated field is calculated in all angles for the direct, indirect and the transmitted part of the Green's tensor. The computed field is then created depending on the placement of the surface, the current method has it placed at $z = 0$, thus when $\pi/2 < \theta < 3/2\pi$ the transmitted part of the field is used and the sum of the direct and indirect radiation is used for the other angles.

CHAPTER 4

Analysis and Results

This chapter presents the results obtained using the implemented MATLAB code discussed in Chapter 3. Section 4.1 contain convergence plots of the induced surface current of a three-dimensional half-wave dipoles, with diameters D of $3, 1, 0.5$ and 0.1 mm. Different excitation types have have been used to produce these figures: plane wave, point source, constant field, and voltage feed. Section 4.2 presents radiation pattern produced by the induced surface currents. In Section 4.3 the results for dipoles located on silicon are presented. The distances between the dipoles and the effect it has on the transmitted radiation has been examined. In each of the above mentioned sections, we have used a dipole length of $L = 10 + D$ cm.

4.1 Induced surface currents on 3D-dipole

As mentioned in Section 2.4, the accuracy of the $\bar{\bar{Z}}$-matrix, and thereby in extension also the surface current $\mathbf{J}$, depends strongly on the number of unknown variables. One method of checking the accuracy of the calculations, is to investigate the convergence of the values of the induced current. The convergence plots in Figure 4.1 showcases the absolute value of the $\hat{\mathbf{y}}$-component of the surface currents induced on a half-wave dipole with a 3 mm diameter. Three different excitation types are presented: plane-wave, point source, and constant field. When incident with a plane wave or a point source, the values converges but the current differs in value around a cross section of the antenna, as seen in Figure 4.1 (a) and (b). This behaviour is further tested by correcting the positions of the center points of triangles and sub-triangle so they match the surface of the antenna. The resulting surface currents obtained by this method are plotted in

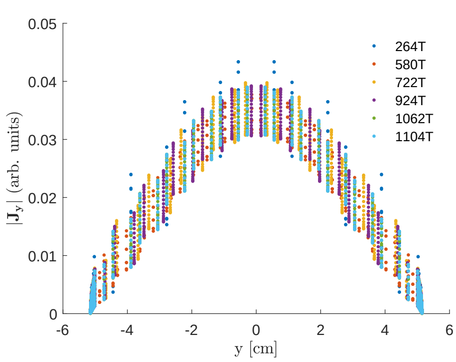

(a) Plane wave

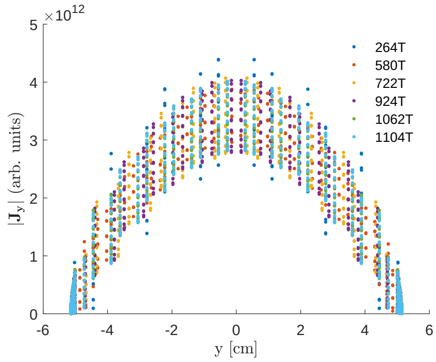

(b) Point source

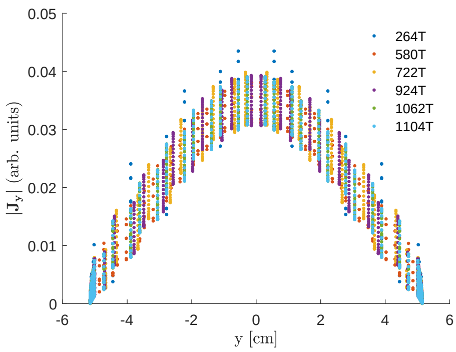

(c) Plane wave w. lift

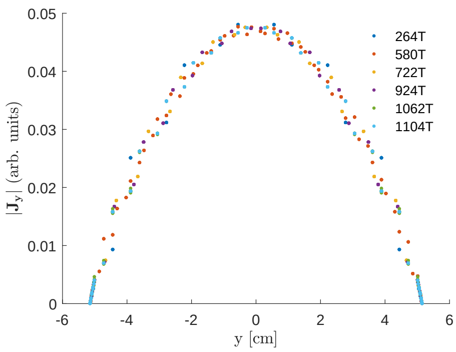

(d) Constant field

FIGURE 4.1 – Induced surface currents of a half-wave dipole with diameter of 3 mm. The different excitation types used are a plane wave, point source and a constant field. The number of triangles used are shown in the legend of each figure. For all excitation types, except the constant field, display variation in surface current values around the cross section of the dipole.

(c), with no noticeable difference. In (d), the use of a constant field produces a very narrow difference in the surface current values around a cross section.

Figure 4.2 shows the $\hat{\mathbf{y}}$-component of the surface currents for half-wave dipoles with diameters of 0.5 and 0.1 mm. As the diameter decreases so does the variation in the cross sectional surface current. However when decreasing the diameter there is an increase in required triangles needed to accurately represent the geometrical surface. The increase in triangles are in all dipole dimensions. The 0.1 mm diameter dipole requires substantially more triangles compared to the 0.5 mm. The figures showcasing the surface currents induced by plane waves from Figures 4.1 and 4.2 are shown side-by-side in Appendix D.

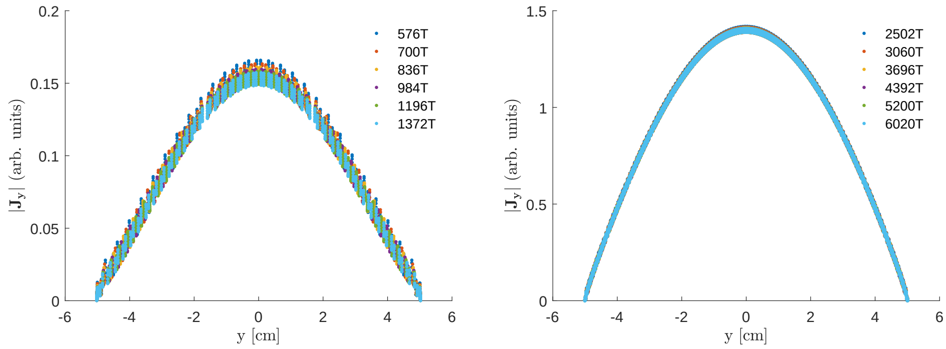

(a) $D = 0.5$ mm (b) $D = 0.1$ mm

FIGURE 4.2 – Surface currents induced by a plane wave vs. antenna length. The cross-sectional variation of the surface currents decreases with smaller diameter. Number of mesh triangles are shown in the legend.

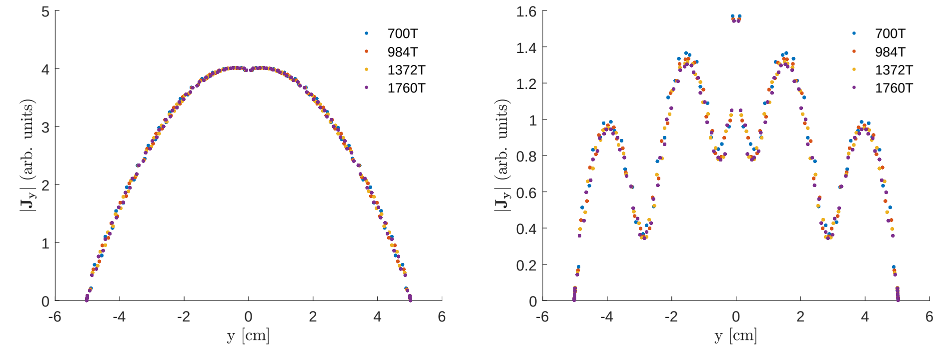

(a) $\lambda = 2L$ (b) $\lambda = L$

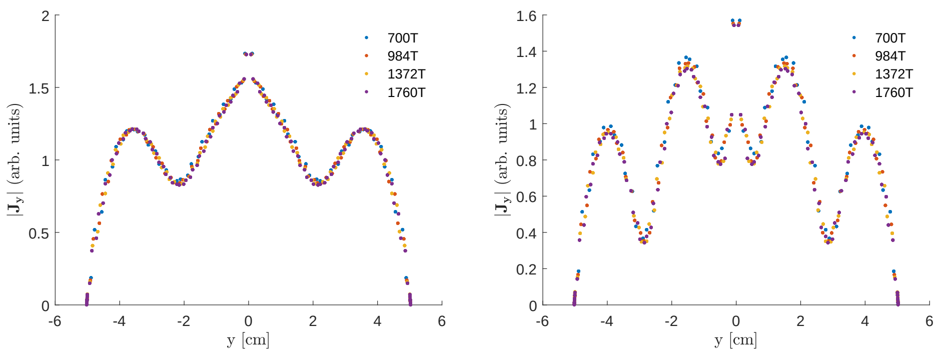

(c) $\lambda = \frac{3}{2}L$ (d) $\lambda = \frac{1}{2}L$

FIGURE 4.3 – Voltage feed induced surface currents for 0.5 mm diameter dipoles. The applied voltage are 1 V. Number of mesh triangles are shown in the legend. Note the nonzero values at $y = 0$ for $\lambda = L$ and $\lambda = \frac{1}{2}L$.

Figure 4.3 shows the surface currents for 0.5 mm diameter dipoles with a voltage feed as excitation source. The voltage feed is applied to the center of the dipole, as described in Subsection 3.1.7. The variation is the cross sectional surface currents are not noticeable, but some nonzero values of the feed current is observed for $\lambda = L$ and $\lambda = \frac{1}{2}L$.

4.2 3D DIPOLE RADIATION

In order to investigate how the variation in the current around a cross section (see Figure 4.1) affect the radiation patterns, we compare the electric field across the dipole in the xy and zy-planes. The 3 mm diameter dipole is selected to be analyzed since it has the most prominent variations. Figure 4.4 shows the electric field across the dipole for the xy and zy-plane in (a) and (b), respectively. At first glance, the field appears to be symmetric around the dipole center in both planes, but a close inspection reveals that the zy-plane show an asymmetry.

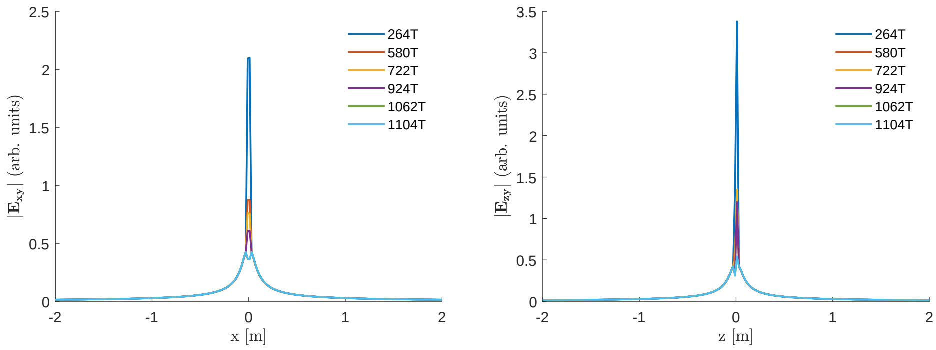

(a) xy-plane (b) zy-plane

FIGURE 4.4 – E-field across a 3 mm diameter dipole. The plane wave excitation source is polarized along $\hat{\mathbf{y}}$ and propagating in the $\hat{\mathbf{z}}$-direction. The xy-plane is fully symmetric, while the zy-plane show a slight asymmetry. Number of mesh triangles are shown in the legend.

TABLE 4.1 – Differences in $|\mathbf{E}_{i,y}|$-value between points at opposite sides of the dipole. The variation in the zy-plane becomes negligible at large distances. The xy-plane is fully symmetric around the dipole center.

Distance from dipole [cm]	± 5.03	± 21.11	± 41.21	± 51.26	± 81.41	± 121.61
$\Delta\|\mathbf{E}_{x,y}\|$	0	0	0	0	0	0
$\Delta\|\mathbf{E}_{z,y}\|$	0.0072	0.0012	0.0003	0.0002	0	0

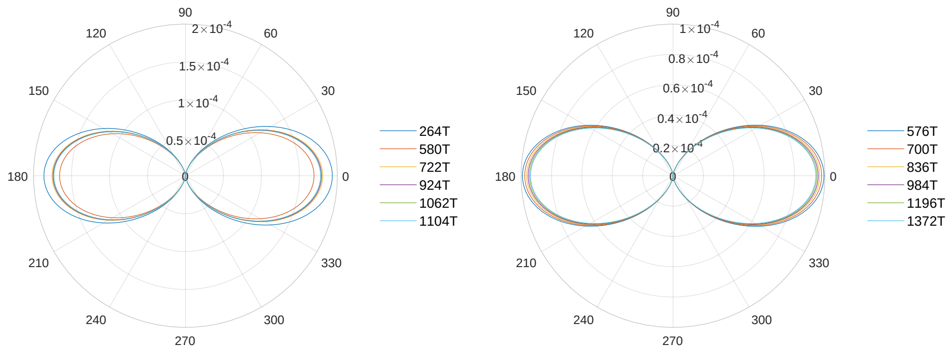

(a) $D = 3$ mm (b) $D = 0.5$ mm

FIGURE 4.5 – Polar plots of the far field radiation for single dipoles diameters of 3 and 0.5 mm in a distance of 10 m. The angles vary in the zy-plane.

The plane wave used as an excitation source is polarized along $\hat{\mathbf{y}}$ and propagates in the $\hat{\mathbf{z}}$-direction. Table 4.1 lists the difference in $|\mathbf{E}_{i,y}|$-values between two points on opposite sides of the dipole. In the xy-plane the field appear symmetric across the dipole, while zy-plane displays a small asymmetry that is most prominent near the dipole.
This representation of the radiated field is however inadequate to establish the directivity of an antenna, and for this purpose polar plots are used. These are presented for dipoles with diameter of 3 and 0.5 mm in Figure 4.5: the angle varies around the zy-plane with 0 being in the immediate positive z-direction. They showcase a deviation in value of the field similar to the cross sectional plots, this difference is more pronounced for the 3mm diameter dipole, which is also in line with the observations from earlier. The plots showcase the expected pattern of a half-wave dipole, and will be used as a baseline comparison to the results when an interface is included.

4.3 DIPOLES ON SI-SUBSTRATE

In order to model a photoconductive antenna, the substrate on which the antennas lie must be included, for this task the Green's tensor for a planar interface, presented in Subsection 2.3.1, is used. In order to carry out this analysis a current density equal to that of a dipole without the interface present have been assumed. In Figure 4.6 the radiation patterns for a single half-wave dipole located in free-space and on a Si-substrate, are shown in (a) and (b), respectively. It is clearly seen that substantially more radiation are coupled into the substrate, and thereby highly changing the directivity of the emitted dipole radiation. Figure 4.7 demonstrates the variation in radiation patterns for half-wave, full-wave, 3/2-wave and 2-wave dipoles on a Si-substrate.

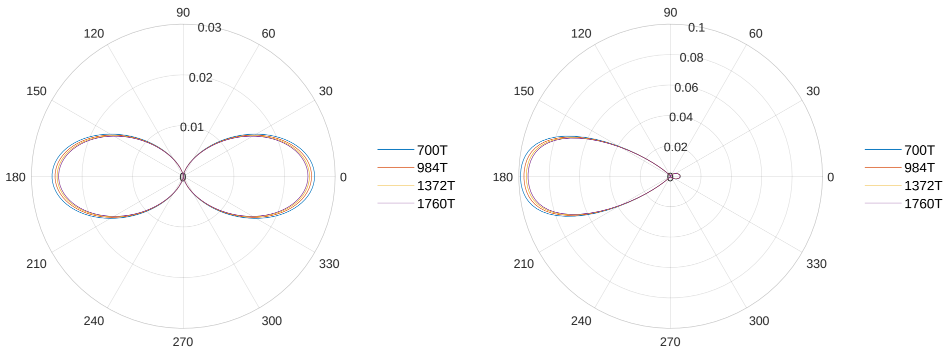

(a) $\frac{1}{2}\lambda$ dipole (b) $\frac{1}{2}\lambda$ dipole w. substrate

FIGURE 4.6 – Angular plot comparison of radiation patterns: (a) Free-space 0.5 mm half-wave dipole w. voltage feed excitation. (b) Same dipole located on Si-substrate. Most of the emitted radiation are coupled into the substrate. Number of mesh triangles are shown in the legend.

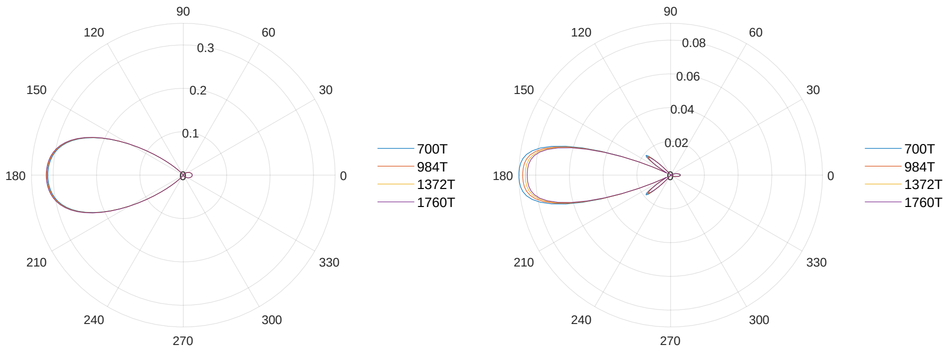

(a) $\frac{1}{2}\lambda$ dipole w. substrate (b) λ dipole w. substrate

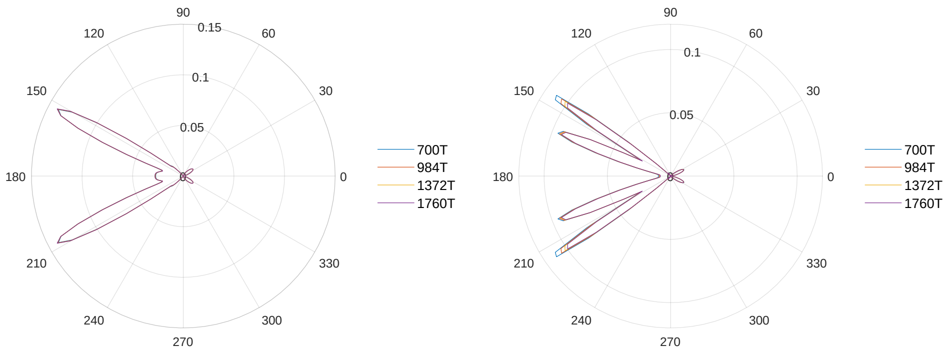

(c) $\frac{3}{2}\lambda$ dipole w. substrate (d) 2λ dipole w. substrate

FIGURE 4.7 – Effects of different wavelength for a dipole on Si-substrate. Number of mesh triangles are shown in the legend.

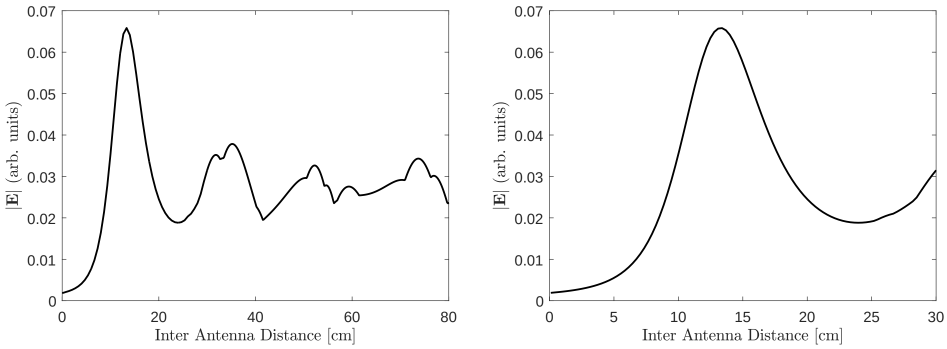

(a) D=0.5mm (b) D=1mm

FIGURE 4.8 – The maximum values of $|\boldsymbol{E}|^2|\mathbf{r}|^2$ plotted as a function of the distance between two dipole antenna.

The radiation patterns partially resembles the radiation from a free-space dipole, as seen in Figure D.2 in Appendix D, but with substantially more radiation coupled into the substrate. The behaviour of coupling radiation into a substrate is of particular interest in the construction of photoconductive antennas, as presented in Chapter 1. As such it is interesting to examine how to increase the directivity of the coupling. This is done by simulating the radiation that results from two and three dipole antenna. By changing the distance between the antenna an optimal inter antenna distance is sought. In the results, that will be presented here, all antenna will be excited by a voltage feed.

In Figure 4.8, the distance between antennas are illustrated for the situation with two dipole antennas placed on the interface. In (a) the results for the 0.5 mm diameter antennas are presented: It can be seen here that the diameter with the highest maximum is a little larger than 10 cm, the actual value is 13.34 cm, this is equivalent to 67% of the wavelength. In Figure 4.9 the radiation pattern is shown. It displays significant radiation in the main lobe located at 180°. However it also displays significant side lobes which could be an unwanted behaviour if the photoconductive antennas are intended to be placed in arrays, as it might interfere destructively with the other configurations in the array. Figure 4.8(b) the same is shown for antennas with diameter of 1 mm. The peak maximum value appears in a similar location to the one for 0.5 mm. The actual value is 13.39 cm which corresponds to 66%. Note that the wavelength depends on the length of the antenna and the diameter influences the length due to the spheres on the ends of the antenna. The radiation pattern for this configuration can be seen in Figure 4.9 (b) where the main lobe is located at 180°. This configuration also displays prominent side lobes.

In Figure 4.10 the inter antenna distance for the situation with three antennas placed on the substrate: (a) displays the results for three dipole antenna with

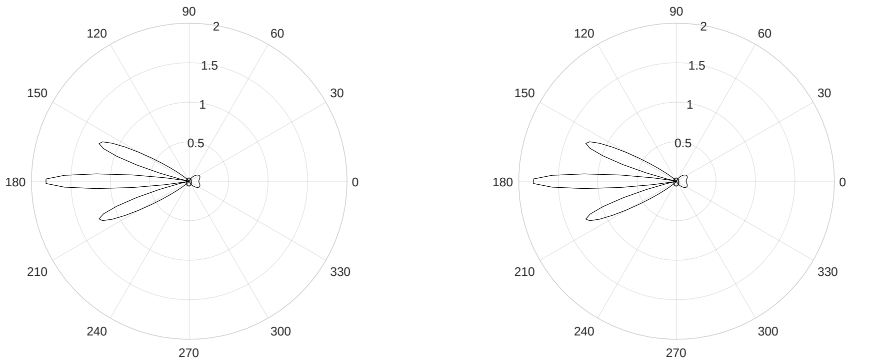

(a) D=0.5mm (b) D=1mm

FIGURE 4.9 – Angular far field radiation patterns for effective inter antenna distance when using two dipole antenna. (a) is for distance of 13.34 cm and (b) is for distance of 13.39 cm.

diameter 0.5 mm, the peak is around 15 cm with the actual value being 14.48 cm. This corresponds to 72% of the wavelength. (b) shows the same but for antenna diameter 1 mm, the peak is at roughly the same spot with a slightly higher value. The actual value is 14.61 cm corresponding to 73% of wavelength.
In Figure 4.11 (a) the angular radiation plot for three dipole antennas with diameter 0.5 mm is shown. It shows a main lobe at 180° as well as prominent side lobes It is worth nothing however that the lobes are more narrow than for the two antenna configuration. In (b), the angular radiation plot is shown for the same configuration but with antenna diameter 1 mm. There are no real difference between the radiation patterns.

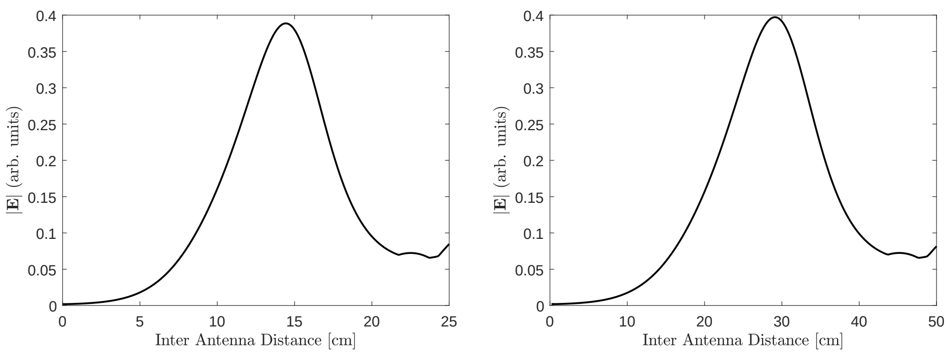

(a) D=0.5mm (b) D=1mm

FIGURE 4.10 – The maximum values of $|\boldsymbol{E}|^2|\mathbf{r}|^2$ plotted as a function of the distance between three dipole antenna.

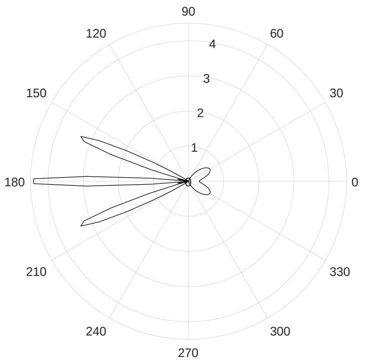

(a) D=0.5mm

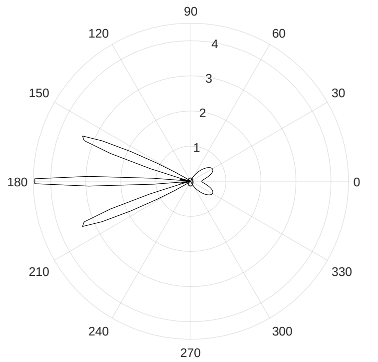

(b) D=1mm

FIGURE 4.11 – Angular far field radiation patterns for effective inter antenna distance when using three dipole antenna. (a) is for distance of 14.48 cm and (b) is for distance of 14.61 cm.

CHAPTER 5

Discussion

The implemented code and the numerical results from Chapters 3-4 will be discussed here. We will discuss the limitations of the code, the methods used, and the validity of the obtained results. The discussion is divided into sections to match the structure of the thesis.

5.1 Induced surface currents

Figures 4.1 (a) and (b) revealed that the induced current on a 3D dipole varied around the cross section when a varying incident field was used as excitation source. For a dipole which is relatively thin compared to the wavelength of a normal-incident wave, polarized along the longitudinal axis of the dipoles, we would not expect the induced current to vary noticeably around the cross section. It was initially considered that the variation could stem from the faceting of the surface, and as an attempt to correct for the variation, the evaluation points used in the numerical integration were moved to the surface. This did not create any noticeable changes in the current distribution, as seen in Figure 4.1 (c). By reducing the diameter of the antenna, the observed variation were reduced. Assuming that the effect is entirely due to the variation of the incident field, it is clear that the cross sectional variation in surface current will be less prominent since the evaluation points are more closely spaced. A trade-off for the reduced variation is the rapid increase in the number of triangles needed to represent the surface accurately due to the increase in surface curvature. Furthermore, when modeling objects in Fusion360 smaller than the 0.1 mm presented, it becomes nearly impossible to check the quality of the meshes.

Ignoring the cross sectional variation, the current appears to converge at around $580, 552, 984$ and 2502 triangles for dipoles with diameters of $3, 1, 0.5$ and 0.1 mm, respectively.
The method of using a voltage feed did produce a current distribution that are more in accord with what we would expect, as seen in Figure 4.1 (d). For the 3 and 0.5 mm diameter dipoles, the current appears to converge at 264 and 700 triangles, respectively, the smallest numbers tested.
The voltage feed method produced some nonzero values at the feeding points when $\lambda = L$ and $\lambda = \frac{1}{2}L$. For an incident wave, these point would normally be zero, but since these are the feed points when using a voltage feed this behavior is expected.

5.2 ANTENNA RADIATION

In order to verify if the variation in the current was due to the incident field's varying across the structure, the cross sections of the electric field over the antenna in the xy and zy-planes was examined. By closely inspecting the two plots in Figure 4.4, it became clear that the dipole radiation were affected by the asymmetric behaviour of the surface currents. The asymmetry is not present in the plane of observation perpendicular to the direction of propagation of the excitation field. This leads us to speculate that the asymmetry mainly stem from the variation in the incident field across the antenna. From Table 4.1 it can bee seen that the variation is negligible when more than three wavelengths away from the dipole.
In order to represent the directivity of the dipole antennas, we made use of polar plots of the far-field radiation. In Figure 4.5 the electric field in the zy-plane show similar asymmetry as the cross sectional plots. The asymmetry became less distinct for smaller diameters, as seen in Figure D.3: For diameters smaller than 3 mm the asymmetry is barely noticeable.

5.3 DIPOLES ON SUBSTRATE

The surface current used to calculate the radiation transmitted into the substrate, is assumed to be the same as if there were no substrate present. This is not the case, as the substrate surface gives rise to a reflection as well as a transmission, which gives the Green's function the additional part of the indirect Green's function. This would likely increase the total current in the antennas. In addition it would probably affect the center antenna in the three antenna configuration the most, thus resulting in a larger difference between the main lobe and the side lobes.
Regarding the excitation method used, in the figures presented, all antennas in the configuration are voltage fed, and on a photoconductive antenna this would not be the case. On a photoconductive antenna, a center point located on the semiconductor between the antennas would be illuminated, produce a current, and

thus begin exciting the antenna. This could, to increase the accuracy of the results, be simulated by applying the voltage feed only to the center antenna, or by employing a point source placed between the two antennas. A correction for this behaviour would likely not result in a change of the found effective distances, as the antennas effectively are the same and the impedance matrix would remain unchanged by this. The change could however be seen in the same way the reflection is thought to have influence, by resulting in a higher current in the center antenna and thus reducing the size of the side lobes.
In addition to this, the antennas should resonate at a higher wavelength, as the refractive index of the substrate would influence the speed of the waves. This could be seen as a new effective refractive index and a new, larger, wavelength could be calculated to account for this change.
In light of this information the distances presented in Table 5.1, most likely overestimate the percentage of the wavelength that should be used for an effective distance, as they are based on a smaller wavelength that does not correct for the substrates presence.

TABLE 5.1 – Effective inter antenna distances for configurations with two and three antennas. Their relation to the wavelength λ is also noted.

	Ant. Dist.	% of λ
Two Antenna 0.5 mm	13.33 cm	67%
Two Antenna 1 mm	13.39 cm	66%
Three Antenna 0.5 mm	14.48 cm	72%
Three Antenna 1 mm	16.61 cm	73%

5.4 MATLAB CODE IN GENERAL

The script implemented for this thesis is reliant on using the method of moments to compute the impedance matrix. In order to do this, the integrals of (2.139) have been evaluated as a 9-point quadrature and a 1-point quadrature for all terms. This has some implications for the accuracy of the calculated $\bar{\bar{Z}}$-matrix, as these only approximate a numerical solution, this approximation could be made more accurate by instead employing an 81-point and a 9-point quadrature. This would still however rely on the same type of approximation and would probably still break down when used on very small triangles, specifically for self-terms. To make the method more reliable for smaller triangles one could do a proper integration using some of MATLAB's integration methods. This would be expensive in time however and should probably only be used for self terms or for evaluating triangles directly next to one another depending on the wanted level of accuracy. This problem could also be addressed by the analytic terms presented in Section 2.5, which would be a faster solution.

In Section 3.3 it was briefly mentioned, that one should consider which parameter to loop over between the amount of triangles and the discretizised steps in the plane of radiation. In this thesis, the resolution used is set to 100 steps per 2 m which gives the matrices a size varying from $40000 - 1000000$, in order to make a swap of loop parameter beneficial the amount of triangles would need to exceed this number. As a reference the largest structure used in this thesis was ≈ 9900 triangles in a Yagi-Uda antenna structure, this parameters for this structure is presented in Table 5.2, with the radiation results in Figure 5.1.

5.4.1 *Yagi-Uda antenna*

Here the results for a nine element Yagi-Uda antenna structure will be presented. This is done in order to demonstrate the capabilities of the script. The Yagi-Uda structure is based on the values presented in [1], scaled to match the wavelength resulting from the choice of dipole length, these measurements can be seen in Table 5.2. The Yagi-Uda antenna is a highly directional antenna array, used

TABLE 5.2 – Scaled Yagi-Uda antenna. Dimensions are based on ones presented by [1].

Element	Ref	1	2	3	4	5	6	7	8
Length [cm]	10.43	9.60	9.61	9.37	9.21	9.11	9.01	8.95	8.91
Position [cm]	0	3.21	4.56	6.99	10.5	14.91	19.95	25.62	32.05

mostly for radio wave communication. This big directivity is observed in the plots for the antenna structure depicted in Figure 5.1. Ultimately however, these results are included to showcase the versatility of the script and thus no analysis is offered.

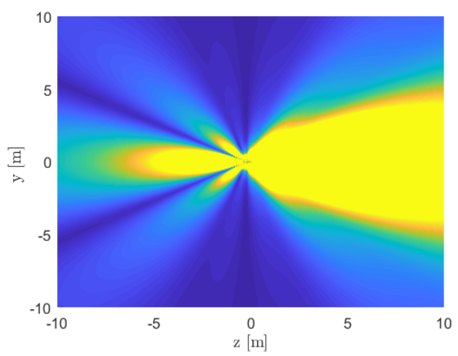

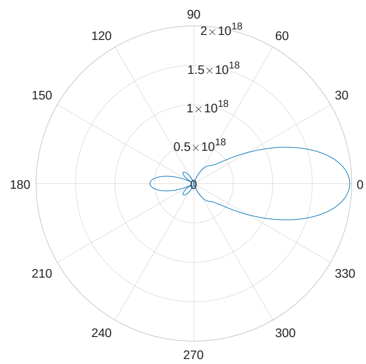

FIGURE 5.1 – Yagi-Uda radiation plots for a voltage feed on the second antenna in the chain. The left plot is the radiated field in the zy-plane, the right plot is for the same plane.

CHAPTER 6

Conclusions

In this chapter, conclusions drawn will be presented on the strengths and weaknesses of the MoM method in regard to the problem statement. Next, a conclusion on based on the results, their general validity, as well as accuracy will be presented. Finally, a general remark will be offered on the fulfillment of the thesis goals.

The MoM showed mixed results in the computation of the current. The results converged for all excitation modes, however, it did showcase a noticeable broadening of the cross sectional surface current when excited by a plane-wave or a point source. While this broadening is thought to be a result of the variation of the excitation fields over the antenna, and as such, is a natural result of employing the MoM on a 3D antenna, no final conclusion could be drawn on whether or not this was actually the case. The current resulting from a voltage feed showed the same current value for a cross section and as such, this excitation method should be safe to employ regardless of the reason for the broadening. Because of this, if one finds it important to account for the current change induced by the inclusion of a substrate, it could be beneficial to use another method. In any case, if one wishes to use the MoM to model this situation some changes need to be applied to the method. This however would likely not result in a significant change to the the radiation patterns, as this was not the case when the substrates influence on the current were neglected.

This observed behaviour in the current resulting from the MoM, influences the likely hood of the results validity. If the broadening indeed is a natural, and intended, result of the method chances are the results hold. Should this not be the case, the results are likely not valuable as the method likely has errors in the implementation. The inter antenna distances presented in Table 5.1 showcase some interesting tendencies in terms of how antennas should be placed in relation to each other: the first is that the radius of the antenna has a limited influence on the optimal distance between antennas. The distance is affected more by the amount of antennas present and seems to, based on limited samples, increase with amount of antennas present. In order to fully optimize the directivity of the radiation, the dimensions wanted for the photoconductive antenna should be known, then one could search for how many antenna can be placed in this area while still maintaining an optimal distance between each other. Additionally as more antennas are added, the distance between them should not necessarily be the same for all.

Overall, the thesis results have shed some light on how the MoM interacts with 3D antennas, how these antenna interact with one another, as well as some information about how radiation transmitted through a substrate could be increased. The thesis have primarily focused on changing the dimensions of antennas by changing their diameter, which showed little influence in terms of good inter antenna distances. It could be of great interest to determine if the % of the wavelength continue to increase as more antenna are added to the structure. In addition it would be interesting to investigate if these % are the same for antenna with different ratios of length to wavelength.

APPENDICES

APPENDIX A

Green's Tensor for a Planar Interface

In Subsection 2.3.1 the Green's tensor for a planar interface in cylindrical coordinates is obtained. The derived expressions of each component of the Green's tensor are included here to provide an overview. For a planar interface between two media at $z = 0$, the Green's tensor is given by

$$\overleftrightarrow{\mathbf{G}}(\mathbf{r},\mathbf{r}') = \begin{cases} \overleftrightarrow{\mathbf{G}}^{(d)}(\mathbf{r},\mathbf{r}') + \overleftrightarrow{\mathbf{G}}^{(i)}(\mathbf{r},\mathbf{r}'), & z > 0, z' > 0\,, \\ \overleftrightarrow{\mathbf{G}}^{(t)}(\mathbf{r},\mathbf{r}'), & z < 0, z > 0\,. \end{cases} \tag{A.1}$$

In cylindrical coordinates, the three components of the Green's tensor are given by

$$\begin{aligned} \overleftrightarrow{\mathbf{G}}^{(d)}(\mathbf{r},\mathbf{r}') = \frac{i}{4\pi}\int \Bigg\{ & \hat{\boldsymbol{\rho}}_r\hat{\boldsymbol{\rho}}_r \left[J_0(k_\rho\rho_r) + \frac{k_\rho^2}{k_1^2} J_0''(k_\rho\rho_r) \right] \\ & + \hat{\boldsymbol{\phi}}_r\hat{\boldsymbol{\phi}}_r \left[J_0(k_\rho\rho_r) + \frac{k_\rho^2}{k_1^2}\frac{J_0'(k_\rho\rho_r)}{k_\rho\rho_r} \right] + \hat{\mathbf{z}}\hat{\mathbf{z}}\,\frac{k_\rho^2}{k_1^2} J_0(k_\rho\rho_r) \\ & + (\hat{\boldsymbol{\rho}}_r\hat{\mathbf{z}} + \hat{\mathbf{z}}\hat{\boldsymbol{\rho}}_r)\, i\frac{k_\rho k_{z_1}}{k_1^2}\frac{z-z'}{|z-z'|} J_0'(k_\rho\rho_r) \Bigg\} \frac{k_\rho}{k_{z_1}} e^{ik_{z_1}|z-z'|}\, dk_\rho\,, \end{aligned} \tag{A.2}$$

$$\overleftrightarrow{\mathbf{G}}^{(i)}(\mathbf{r},\mathbf{r}') = \frac{i}{4\pi}\int_0^\infty \Bigg\{ -r^{(s)}(k_\rho)\left(\hat{\boldsymbol{\rho}}_r\hat{\boldsymbol{\rho}}_r\,\frac{J_0'(k_\rho\rho_r)}{k_\rho\rho_r} + \hat{\boldsymbol{\phi}}_r\hat{\boldsymbol{\phi}}_r\,J_0''(k_\rho\rho_r)\right) \tag{A.3}$$
$$+\,r^{(p)}(k_\rho)\left(\hat{\boldsymbol{\rho}}_r\hat{\boldsymbol{\rho}}_r\,\frac{k_{z_1}^2}{k_1^2}J_0''(k_\rho\rho) + \hat{\boldsymbol{\phi}}_r\hat{\boldsymbol{\phi}}_r\,\frac{k_{z_1}^2}{k_1^2}\frac{J_0'(k_\rho\rho_r)}{k_\rho\rho_r} + \hat{\mathbf{z}}\hat{\mathbf{z}}\,\frac{k_\rho^2}{k_1^2}J_0(k_\rho\rho_r)\right.$$
$$\left.+\,(\hat{\boldsymbol{\rho}}_R\hat{\mathbf{z}} - \hat{\mathbf{z}}\hat{\boldsymbol{\rho}}_r)\,i\frac{k_\rho k_{z_1}}{k_1^2}J_0'(k_\rho\rho_r)\right)\Bigg\}\,\frac{k_\rho}{k_{z_1}}e^{ik_{z_1}(z+z')}\,dk_\rho\,,$$

and

$$\overleftrightarrow{\mathbf{G}}^{(t)}(\mathbf{r},\mathbf{r}') = \frac{i}{4\pi}\int_0^\infty \Bigg\{ -t^{(s)}(k_\rho)\left(\hat{\boldsymbol{\rho}}_r\hat{\boldsymbol{\rho}}_r\,\frac{J_0'(k_\rho\rho_r)}{k_\rho\rho_r} - \hat{\boldsymbol{\phi}}_r\hat{\boldsymbol{\phi}}_r\,J_0''(k_\rho\rho_r)\right) \tag{A.4}$$
$$-\,t^{(p)}(k_\rho)\left(\hat{\boldsymbol{\rho}}_r\hat{\boldsymbol{\rho}}_r\,\frac{k_{z_1}k_{z_2}}{k_1^2}J_0''(k_\rho\rho_r) + \hat{\boldsymbol{\phi}}_r\hat{\boldsymbol{\phi}}_r\,\frac{k_{z_1}k_{z_2}}{k_1^2}\frac{J_0'(k_\rho\rho_r)}{k_\rho\rho_r} + \hat{\mathbf{z}}\hat{\mathbf{z}}\,\frac{k_\rho^2}{k_1^2}J_0(k_\rho\rho_r)\right.$$
$$\left.-(\hat{\boldsymbol{\rho}}_r\hat{\mathbf{z}}\frac{k_{z_2}}{k_{z_1}} + \hat{\mathbf{z}}\hat{\boldsymbol{\rho}}_r)\,i\frac{k_\rho k_{z_1}}{k_1^2}J_0'(k_\rho\rho_r)\right)\Bigg\}\,\frac{k_\rho}{k_{z_1}}e^{ik_{z_1}z'}e^{-ik_{z_2}z}\,dk_\rho\,,$$

where

$$r^{(p)}(k_\rho) = \frac{\varepsilon_2 k_{z_1} - \varepsilon_1 k_{z_2}}{\varepsilon_2 k_{z_1} + \varepsilon_1 k_{z_2}}\,, \tag{A.5a}$$

$$t^{(p)}(k_\rho) = 1 + r^{(p)}(k_\rho)\,, \tag{A.5b}$$

$$r^{(s)}(k_\rho) = \frac{k_{z_1} - k_{z_2}}{k_{z_1} + k_{z_2}}\,, \tag{A.5c}$$

$$t^{(s)}(k_\rho) = 1 + r^{(s)}(k_\rho)\,. \tag{A.5d}$$

It should be noted that ρ, $\hat{\boldsymbol{\rho}}$ and $\hat{\boldsymbol{\phi}}$ are relative with respect to the distance between $\mathbf{r}$ and $\mathbf{r}'$.

APPENDIX B

Integral Identity

The following proof seek to justify the use of the identity given by Eq. (B.1). This identity is used in order to rewrite Eq. (2.134) in order to obtain an alternative form of the electric field integral equation, used in Section 2.5. We thus wish to proof the following:

$$\nabla\nabla \cdot \iiint_V \mathbf{J}(\mathbf{r}')g(\mathbf{r},\mathbf{r}')\,d\mathbf{r}' = \nabla \iiint_V g(\mathbf{r},\mathbf{r}')\Big[\nabla' \cdot \mathbf{J}(\mathbf{r}')\Big]d\mathbf{r}\,. \tag{B.1}$$

Consider the volume integral $\mathcal{I}(\mathbf{r})$ given by

$$\mathcal{I}(\mathbf{r}) = \nabla\nabla \cdot \iiint_V \mathbf{J}(\mathbf{r}')g(\mathbf{r},\mathbf{r}')\,d\mathbf{r}'\,. \tag{B.2}$$

By utilizing the vector identity,

$$\nabla \cdot \Big[\mathbf{J}(\mathbf{r}')g(\mathbf{r},\mathbf{r}')\Big] = g(\mathbf{r},\mathbf{r}')\Big[\nabla \cdot \mathbf{J}(\mathbf{r}')\Big] + \mathbf{J}(\mathbf{r}') \cdot \Big[\nabla g(\mathbf{r},\mathbf{r}')\Big]\,, \tag{B.3}$$

Eq. (B.2) can be rewritten as

$$\mathcal{I}(\mathbf{r}) = \nabla \iiint_V \mathbf{J}(\mathbf{r}') \cdot \nabla g(\mathbf{r},\mathbf{r}')\,d\mathbf{r}'\,, \tag{B.4}$$

where $[\nabla \cdot \mathbf{J}(\mathbf{r}')] = \mathbf{0}$, since $\mathbf{J}(\mathbf{r}')$ has no $\mathbf{r}'$ dependency. Due to the symmetry of the Green's function, the following relationship can be used,

$$\nabla g(\mathbf{r},\mathbf{r}') = -\nabla' g(\mathbf{r},\mathbf{r}')\,, \tag{B.5}$$

where ∇' indicate the gradient with respect to $\mathbf{r}'$. By using Eq. (B.5), Eq. (B.4) can be stated as

$$\mathcal{I}(\mathbf{r}) = -\nabla \iiint_V \mathbf{J}(\mathbf{r}') \cdot \nabla' g(\mathbf{r}, \mathbf{r}')\, d\mathbf{r}' \,. \tag{B.6}$$

By using the vector identity given by Eq. (B.3) again, Eq. (B.6) becomes

$$\mathcal{I}(\mathbf{r}) = \nabla \iiint_V g(\mathbf{r}, \mathbf{r}') \Big[\nabla' \cdot \mathbf{J}(\mathbf{r}')\Big] d\mathbf{r}' - \nabla \iiint_V \nabla' \cdot \Big[\mathbf{J}(\mathbf{r}') g(\mathbf{r}, \mathbf{r}')\Big] d\mathbf{r}' \,. \tag{B.7}$$

By applying Gauss's theorem, the second volume integral can be converted into an integral over an surface surrounding the volume, yielding

$$\begin{aligned} \mathcal{I}(\mathbf{r}) &= \nabla \iiint_V g(\mathbf{r}, \mathbf{r}') \Big[\nabla' \cdot \mathbf{J}(\mathbf{r}')\Big] d\mathbf{r}' - \nabla \iint_S \Big[\mathbf{J}(\mathbf{r}') g(\mathbf{r}, \mathbf{r}')\Big] \cdot \hat{n}\, d\mathbf{r}' \\ &= \nabla \iiint_V g(\mathbf{r}, \mathbf{r}') \Big[\nabla' \cdot \mathbf{J}(\mathbf{r}')\Big] d\mathbf{r}' \,, \end{aligned} \tag{B.8}$$

where the surface integral equals zero, since $\mathbf{J}(\mathbf{r}')$ is enclosed by the volume contained inside the surface. By comparing Eq. (B.2) and Eq. (B.8), the identity given by Eq. (B.1) is proven.

APPENDIX C

Matlab Code

C.1 MoM loop based

```
function [Z,  a, b] = MoM(w, mu, t, EdgeList, BasisLA, RhoP, RhoM,...
RhoP_, RhoM_, Center, k, SubTri, Ei, eps0)

    Z = zeros(length(EdgeList),length(EdgeList))...
    +1i*zeros(length(EdgeList),length(EdgeList));
    %Returns array with indices corresponding to edgenumber and the
    %corresponding plus and minus triangle repsectively
    [PlusTri, MinusTri] = ArbitraryAntenna.PMTri(t, EdgeList);

    SubAmount = size(SubTri);
    Quad = SubAmount(1);

    for m=1:length(EdgeList)
        mPdist = sqrt(sum((Center(PlusTri(m),:)-SubTri).^2,2));
        mMdist = sqrt(sum((Center(MinusTri(m),:)-SubTri).^2,2));
        rhomP = RhoP(m,:);
        rhomM = RhoM(m,:);

        for n=1:length(EdgeList)
            rhonP_ = RhoP_(:,:,n);
            rhonM_ = RhoM_(:,:,n);

            gmPnP = exp(-1i*k*mPdist(:,:,PlusTri(n)))...
            ./mPdist(:,:,PlusTri(n));
            gmMnP = exp(-1i*k*mMdist(:,:,PlusTri(n)))...
            ./mMdist(:,:,PlusTri(n));

```

```
            gmPnM = exp(-1i*k*mPdist(:,:,MinusTri(n)))...
            ./mPdist(:,:,MinusTri(n));
            gmMnM = exp(-1i*k*mMdist(:,:,MinusTri(n)))...
            ./mMdist(:,:,MinusTri(n));

            AmnP = mu/(4*pi)*...
            (BasisLA(n,2)*sum(rhonP_.*gmPnP/(2*Quad))...
            +BasisLA(n,2)*sum(rhonM_.*gmPnM/(2*Quad)));
            AmnM = mu/(4*pi)*...
            (BasisLA(n,2)*sum(rhonP_.*gmMnP/(2*Quad))...
            +BasisLA(n,2)*sum(rhonM_.*gmMnM/(2*Quad)));

            PhiP = -1/(4*pi*1i*w*eps0)*...
            (BasisLA(n,2)*sum(gmPnP)/Quad ...
             -BasisLA(n,2)*sum(gmPnM)/Quad);
            PhiM = -1/(4*pi*1i*w*eps0)*...
            (BasisLA(n,2)*sum(gmMnP)/Quad...
            -BasisLA(n,2)*sum(gmMnM)/Quad);

            Z(m,n) = BasisLA(m,2)*(1i*w*(dot(AmnP,rhomP)/2 ...
            +dot(AmnM,rhomM)/2)+PhiM-PhiP);
            end
        end
        b = BasisLA(:,2).*(dot(Ei(PlusTri,:),RhoP,2)/2 ...
        +dot(Ei(MinusTri,:),RhoM,2)/2);

        a = Z\b;
    end
```

C.2 MOM VECTORIZED

```
function [Z, a, b] = MoMVectorized(w, mu, t, p, EdgeList, BasisLA,...
RhoP, RhoM, RhoP_, RhoM_, Basis, Center, k, SubTri, Ei,...
Reflector, GIxx, GIxy, GIxz, GIyx, GIyy, GIyz, ...
GIzx, GIzy, GIzz, eps0)
    % alocating space
    Z = zeros(length(EdgeList),length(EdgeList))...
    +1i*zeros(length(EdgeList),length(EdgeList));

    SubAmount = size(SubTri);
    Quad = SubAmount(1);

    EdgesTotal = length(EdgeList);
    %Returns array with indices corresponding to edgenumber and the
    %corresponding plus and minus triangle repsectively
    [PlusTri, MinusTri] = ArbitraryAntenna.PMTri(t, EdgeList);
    %Analytical Selftems
    [BasisAnalytic, DistAnalytic] = ArbitraryAntenna.SelfTermInt...
    (t, p, k);
```

```

    for m=1:EdgesTotal
        mPdist = sqrt(sum((Center(PlusTri(m),:)-SubTri).^2,2));
        mMdist = sqrt(sum((Center(MinusTri(m),:)-SubTri).^2,2));
        rhomP = repmat(RhoP(m,:),length(EdgeList),1);
        rhomM = repmat(RhoM(m,:),length(EdgeList),1);

        SamenPmP = find(PlusTri - PlusTri(m) == 0);
        SamenMmP = find(MinusTri - PlusTri(m) == 0);
        SamenMmM = find(MinusTri - MinusTri(m) == 0);
        SamenPmM = find(PlusTri - MinusTri(m) == 0);

        gmPnP = exp(1i*k*mPdist(:,:,PlusTri))...
        ./mPdist(:,:,PlusTri);
        gmMnP = exp(1i*k*mMdist(:,:,PlusTri))...
        ./mMdist(:,:,PlusTri);

        gmPnM = exp(1i*k*mPdist(:,:,MinusTri))...
        ./mPdist(:,:,MinusTri);
        gmMnM = exp(1i*k*mMdist(:,:,MinusTri))...
        ./mMdist(:,:,MinusTri);

        Acnst = mu/(4*pi);
        PPA = permute(sum(RhoP_.*gmPnP/(2*Quad)),[3 2 1]);
        MPA = permute(sum(RhoM_.*gmPnM/(2*Quad)),[3 2 1]);
        PMA = permute(sum(RhoP_.*gmMnP/(2*Quad)),[3 2 1]);
        MMA = permute(sum(RhoM_.*gmMnM/(2*Quad)),[3 2 1]);

        AmnP = Acnst.*BasisLA(:,2).*(PPA+MPA);
        AmnM = Acnst.*BasisLA(:,2).*(PMA+MMA);

        Pcnst = -1/(4*pi*1i*w*eps0);
        PPPhi = permute(sum(gmPnP),[3 2 1])/(Quad);
        PMPhi = permute(sum(gmPnM),[3 2 1])/(Quad);
        MPPhi = permute(sum(gmMnP),[3 2 1])/(Quad);
        MMPhi = permute(sum(gmMnM),[3 2 1])/(Quad);

        PPPhi(SamenPmP) = DistAnalytic(PlusTri(m));
        PMPhi(SamenMmP) = DistAnalytic(PlusTri(m));
        MMPhi(SamenMmM) = DistAnalytic(MinusTri(m));
        MPPhi(SamenPmM) = DistAnalytic(MinusTri(m));

        PhiP = Pcnst*BasisLA(:,2).*(PPPhi-PMPhi);
        PhiM = Pcnst*BasisLA(:,2).*(MPPhi-MMPhi);

        if Reflector
            % Attempt at implementing reflection from surface in
            GIx = [GIxx(:,PlusTri(m),:) ...
            GIxy(:,PlusTri(m),:) GIxz(:,PlusTri(m),:)];

            GIy = [GIyx(:,PlusTri(m),:) ...
            GIyy(:,PlusTri(m),:) GIyz(:,PlusTri(m),:)];

            GIz = [GIzx(:,PlusTri(m),:) ...
```

```
            GIzy(:,PlusTri(m),:) GIzz(:,PlusTri(m),:)];
            GImP = GIx + GIy + GIz;

            GIx = [GIxx(:,MinusTri(m),:) ...
            GIxy(:,MinusTri(m),:) GIxz(:,MinusTri(m),:)];

            GIy = [GIyx(:,MinusTri(m),:) ...
            GIyy(:,MinusTri(m),:) GIyz(:,MinusTri(m),:)];

            GIz = [GIzx(:,MinusTri(m),:) ...
            GIzy(:,MinusTri(m),:) GIzz(:,MinusTri(m),:)];
            GImM = GIx+GIy+GIz;

            GImPnP = GImP(:,:,PlusTri);
            GImMnP = GImM(:,:,MinusTri);

            GImPnM = GImP(:,:,PlusTri);
            GImMnM = GImM(:,:,MinusTri);

            Z(m,:) = (1i*w*mu/(4*pi).*BasisLA(:,2).*BasisLA(m,2).*(dot(permute(sum(RhoP_.*GIm
            +permute(sum(RhoM_.*GImPnM/(2*Quad)),[3 2 1]),rhomP,2)+...
            dot(permute(sum(RhoP_.*GImMnP/(2*Quad)),[3 2 1])...
            +permute(sum(RhoM_.*GImMnM/(2*Quad)),[3 2 1]),rhomM,2))).';
        end

        PlusDotProd = dot(AmnP,rhomP,2);
        MinusDotProd = dot(AmnM,rhomM,2);

        Z(m,:) = BasisLA(m,2).*(1i*w*(PlusDotProd/2 ...
        +MinusDotProd/2)+PhiM-PhiP).'+Z(m,:);
    end

    b = BasisLA(:,2).*(dot(Ei(PlusTri,:),RhoP,2)/2 ...
    +dot(Ei(MinusTri,:),RhoM,2)/2);

    %System solution
    a=Z\b;
end
```

C.3 RADIATED E-FIELD

```
function [Exy, Exz, Ezy, xrange, yrange, zrange, Exyx, Exzx, Eyzx, ...
Exyy, Exzy, Eyzy, Exyz, Exzz, Eyzz] = EField(Center, ...
w, mu, k0, J, xmin, xmax, ymin, ymax, zmin, zmax, ...
steps, Area, Reflect, xsurf, n, lambda)

    kR = 2*pi/(lambda*n);
    xrange = linspace(xmin, xmax, steps);
    yrange = linspace(ymin, ymax, steps);
```

```
zrange = linspace(zmin, zmax, steps);

Exy = zeros(steps, steps);
Exyx = Exy; Exyy = Exy; Exyz = Exy;
Exz = zeros(steps,steps);
Exzx = Exz; Exzy = Exz; Exzz = Exz;
Eyz = zeros(steps,steps);
Eyzx = Eyz; Eyzy = Eyz; Eyzz = Eyz;

for j=1:3
    if j == 1
        rx = (xrange-Center(:,1));
        ry = (yrange-Center(:,2));
        rz = (0-Center(:,3));
    elseif j==2
        rx = (xrange-Center(:,1));
        ry = (0-Center(:,2));
        rz = (zrange-Center(:,3));
    else
        rx = (0-Center(:,1));
        ry = (yrange-Center(:,2));
        rz = (zrange-Center(:,3));
    end

    for i=1:length(Center)
        if j == 1
            %xy
            Rx = repmat(rx(i,:)',1,steps);
            Ry = repmat(ry(i,:),steps,1);
            Rz = repmat(rz(i),steps,steps);
            r = sqrt(Rx.^2+Ry.^2+Rz.^2);
            surfside = find(rz(i,:)>=xsurf);
            k = zeros(steps,steps);
            k(:,:) = k0;

            if Reflect
                k(surfside,:) = kR;
            end

            g = exp(1i.*k.*r)./(4*pi*r);
            G1 = (1+1i./(k.*r)-1./(k.*r).^2);
            G2 = (1+3i./(k.*r)-3./(k.*r).^2);

            RR = Rx.*Rx;
            Gxx = (G1-(RR./r.^2).*G2).*g;
            RR = Ry.*Rx;
            Gxy = (-(RR./r.^2).*G2).*g;
            RR = Rz.*Rx;
            Gxz = (-(RR./r.^2).*G2).*g;
            Exyx = Exyx + 1i.*w.*mu.*...
            (Gxx.*J(i,1) + Gxy.*J(i,2) + Gxz.*J(i,3))*Area(i);

            RR = Ry.*Rx;
            Gyx = (-(RR./r.^2).*G2).*g;
```

```
                RR = Ry.*Ry;
                Gyy = (G1-(RR./r.^2).*G2).*g;
                RR = Ry.*Rz;
                Gyz = (-(RR./r.^2).*G2).*g;
                Exyy = Exyy + 1i.*w.*mu.*...
                (Gyx.*J(i,1) + Gyy.*J(i,2) + Gyz.*J(i,3))*Area(i);

                RR = Rz.*Rx;
                Gzx = (-(RR./r.^2).*G2).*g;
                RR = Rz.*Ry;
                Gzy = (-(RR./r.^2).*G2).*g;
                RR = Rz.*Rz;
                Gzz = (G1-(RR./r.^2).*G2).*g;
                Exyz = Exyz + 1i.*w.*mu.*...
                (Gzx.*J(i,1) + Gzy.*J(i,2) + Gzz.*J(i,3))*Area(i);

            elseif j==2
                %xz
                Rx = repmat(rx(i,:)',1,steps);
                Ry = repmat(ry(i,:),steps,steps);
                Rz = repmat(rz(i,:),steps,1);
                r = sqrt(Rx.^2+Ry.^2+Rz.^2);
                surfside = find(rz(i,:)>=xsurf);
                k = zeros(steps,steps);
                k(:,:) = k0;

                if Reflect
                    k(surfside,:) = kR;
                end

                g = exp(1i.*k.*r)./(4*pi*r);
                G1 = (1+1i./(k.*r)-1./(k.*r).^2);
                G2 = (1+3i./(k.*r)-3./(k.*r).^2);

                RR = Rx.*Rx;
                Gxx = (G1-(RR./r.^2).*G2).*g;
                RR = Rx.*Ry;
                Gxy = (-(RR./r.^2).*G2).*g;
                RR = Rx.*Rz;
                Gxz = (-(RR./r.^2).*G2).*g;
                Exzx = Exzx + 1i.*w.*mu.*...
                (Gxx.*J(i,1) + Gxy.*J(i,2) + Gxz.*J(i,3))*Area(i);

                RR = Ry.*Rx;
                Gyx = (-(RR./r.^2).*G2).*g;
                RR = Ry.*Ry;
                Gyy = (G1-(RR./r.^2).*G2).*g;
                RR = Ry.*Rz;
                Gyz = (-(RR./r.^2).*G2).*g;
                Exzy = Exzy + 1i.*w.*mu.*...
                (Gyx.*J(i,1) + Gyy.*J(i,2) + Gyz.*J(i,3))*Area(i);

                RR = Rz.*Rx;
                Gzx = (-(RR./r.^2).*G2).*g;
```

```
                RR = Rz.*Ry;
                Gzy = (-(RR./r.^2).*G2).*g;
                RR = Rz.*Rz;
                Gzz = (G1-(RR./r.^2).*G2).*g;
                Exzz = Exzz + 1i.*w.*mu.*...
                (Gzx.*J(i,1) + Gzy.*J(i,2) + Gzz.*J(i,3))*Area(i);

            else
                %yz
                Rx = repmat(rx(i,:),steps,steps);
                Ry = repmat(ry(i,:),steps,1);
                Rz = repmat(rz(i,:)',1,steps);
                r = sqrt(Rx.^2+Ry.^2+Rz.^2);
                surfside = find(rz(i,:)>=xsurf);
                k = zeros(steps,steps);
                k(:,:) = k0;

                if Reflect
                    k(surfside,:) = kR;
                end

                g = exp(1i.*k.*r)./(4*pi*r);
                G1 = (1+1i./(k.*r)-1./(k.*r).^2);
                G2 = (1+3i./(k.*r)-3./(k.*r).^2);

                RR = Rx.*Rx;
                Gxx = (G1-(RR./r.^2).*G2).*g;
                RR = Rx.*Ry;
                Gxy = (-(RR./r.^2).*G2).*g;
                RR = Rx.*Rz;
                Gxz = (-(RR./r.^2).*G2).*g;
                Eyzx = Eyzx + 1i.*w.*mu.*...
                (Gxx.*J(i,1) + Gxy.*J(i,2) + Gxz.*J(i,3))*Area(i);

                RR = Ry.*Rx;
                Gyx = (-(RR./r.^2).*G2).*g;
                RR = Ry.*Ry;
                Gyy = (G1-(RR./r.^2).*G2).*g;
                RR = Ry.*Rz;
                Gyz = (-(RR./r.^2).*G2).*g;
                Eyzy = Eyzy + 1i.*w.*mu.*...
                (Gyx.*J(i,1) + Gyy.*J(i,2) + Gyz.*J(i,3))*Area(i);

                RR = Rz.*Rx;
                Gzx = (-(RR./r.^2).*G2).*g;
                RR = Rz.*Ry;
                Gzy = (-(RR./r.^2).*G2).*g;
                RR = Rz.*Rz;
                Gzz = (G1-(RR./r.^2).*G2).*g;
                Eyzz = Eyzz + 1i.*w.*mu.*...
                (Gzx.*J(i,1) + Gzy.*J(i,2) + Gzz.*J(i,3))*Area(i);
            end
        end
    end
```

```
    Exy = sqrt(Exyx.^2+Exyy.^2+Exyz.^2);
    Exz = sqrt(Exzx.^2+Exzy.^2+Exzz.^2);
    Ezy = sqrt(Eyzx.^2+Eyzy.^2+Eyzz.^2);
end
```

C.4 ANGULAR FAR-FIELD

```
function [Esc] = AngularFarFieldSurf(w, mu, k, r,...
Center, J, steps, Area, eps2, eps1, n)

    phi = pi/2;
    theta = linspace(0, 2*pi, steps)';

    under = theta>=pi/2;
    over = theta<=3/2*pi;
    UseTrans = logical(under.*over);

    eps2=eps2*eps1;
    k1 = k;
    k2 = k*n;
    kz1 = k1*cos(theta);
    krho = k1*sin(theta);
    krho2 = k2*sin(theta);
    kz2 = k2*cos(theta);

    refS = (kz1-kz2)./(kz1+kz2);
    refP = eps2.*kz1-eps1.*kz2)./(eps2.*kz1+eps1.*kz2);
    traS = 1+refS;
    traP = 1+refP;

    xH = [1, 0, 0];
    yH = [0, 1, 0];
    zH = [0, 0, 1];
    %%
    PhiH = -xH.*sin(phi)+yH.*cos(phi);
    thetaHD = (xH.*cos(phi)+yH.*sin(phi)).*cos(theta)-zH.*sin(theta);

    thetaHT = ...
    xH.*cos(phi).*(cos(theta).*kz1.*kz2/k1^2 ...
    -sin(theta).*kz1.*krho2/k1^2) ...
    +yH.*sin(phi).*(cos(theta).*kz1.*kz2/k1^2 ...
    -sin(theta).*kz1.*krho2/k1^2) ...
    +zH.*(-sin(theta).*krho2.^2/k1^2 ...
    +cos(theta).*kz2.*krho2/k1^2);

    rHatT = ...
    xH.*cos(phi).*(sin(theta).*kz1.*kz2/k1^2 ...
    +cos(theta).*kz1.*krho2/k1^2) ...
    +yH.*sin(phi).*(sin(theta).*kz1.*kz2/k1^2 ...
```

```
    +cos(theta).*kz1.*krho2/k1^2) ...
    +zH.*(cos(theta).*krho2.^2/k1^2 ...
    +sin(theta).*kz2.*krho2/k1^2);

    thetaHI = zH.*krho/k1+xH.*cos(phi).*kz1/k1+yH.*sin(phi).*kz1/k1;

    rHat = (xH.*cos(phi)+yH.*sin(phi)).*sin(theta)+zH.*cos(theta);

    rhoH = xH.*cos(theta)+yH.*sin(theta);
    %%
    EscThetaD = 1:steps; EscThetaD(:) =0;
    EscPhiD = 1:steps; EscPhiD(:) = 0;

    EscThetaI = 1:steps; EscThetaI(:) =0;
    EscPhiI = 1:steps; EscPhiI(:) = 0;

    EscThetaT = 1:steps; EscThetaT(:) =0;
    EscPhiT = 1:steps; EscPhiT(:) = 0;
    EscrT = 1:steps; EscrT(:) = 0;

    %%
    for i=1:length(Center)
        z = Center(i,3);

        DirectGreens = (exp(1i*k*r)/(4*pi*r))...
        .*exp(-1i*k*dot(rHat,repmat(Center(i,:),length(rHat),1),2));
        DirectGreensTheta =        DirectGreens.*thetaHD;
        DirectGreensPhi = DirectGreens.*phiH;

        DirectGreensTheta = ...
        dot(DirectGreensTheta, repmat(J(i,:),steps,1),2);
        DirectGreensPhi = ...
        dot(DirectGreensPhi, repmat(J(i,:),steps,1),2);

        %%
        IDGreensBase = exp(1i*k1*r)/(4*pi*r) .*exp(-1i*krho...
        .*dot(rhoH,repmat(Center(i,:),length(rhoH),1),2))...
        .*exp(1i*kz1.*z);

        IDGreensBaseTheta = IDGreensBase.*thetaHI;
        IDGreensBasePhi = IDGreensBase.*phiH;

        IndirectGreensPhi =...
        dot(IDGreensBasePhi,repmat(J(i,:),steps,1),2).*refS;

        IndirectGreensTheta =...
        -refP.*dot(IDGreensBaseTheta,repmat(J(i,:),steps,1),2);
        %%
        TransGreensBase = kz2./kz1.*exp(1i*k2*r)/(4*pi*r)...
        .*exp(1i*kz1.*z).*exp(-1i*krho2...
        .*dot(rhoH,repmat(Center(i,:),length(rhoH),1),2));

        TransGreensPhi = TransGreensBase .*phiH;
        TransGreensTheta = TransGreensBase .*thetaHT;
```

```
        TransGreensR = TransGreensBase .*rHatT;

        TransmitGreensPhi = ...
        dot(TransGreensPhi,repmat(J(i,:),steps,1),2).*traS;

        TransmitGreensTheta = traP.*eps1/eps2 ...
        .* dot(TransGreensTheta,repmat(J(i,:),steps,1),2);

        TransmitGreensR = ...
        dot(TransGreensR,repmat(J(i,:),steps,1),2).*traP.*eps1/eps2;
        %%
        EscThetaD = -1i*w*mu*Area(i).*DirectGreensTheta.' ...
        + EscThetaD;
        EscPhiD = -1i*w*mu*Area(i).*DirectGreensPhi.' ...
        + EscPhiD;

        EscThetaI = -1i*w*mu*Area(i).*IndirectGreensTheta.' ...
        + EscThetaI;
        EscPhiI = -1i*w*mu*Area(i).*IndirectGreensPhi.' ...
        + EscPhiI;

        EscThetaT = -1i*w*mu*Area(i).*TransmitGreensTheta.' ...
        + EscThetaT;
        EscPhiT = -1i*w*mu*Area(i).*TransmitGreensPhi.' ...
        + EscPhiT;
        EscrT = -1i*w*mu*Area(i).*TransmitGreensR.' ...
        + EscrT;
    end

    Esc = abs(EscPhiD+EscPhiI).^2+abs(EscThetaD+EscThetaI).^2;
    EscT = abs(EscPhiT).^2+abs(EscThetaT).^2+abs(EscrT).^2;

    Esc(UseTrans) = EscT(UseTrans);

    figure(7)
    polarplot(theta, 1/2*Esc*r^2);
end
```

APPENDIX D

Figures

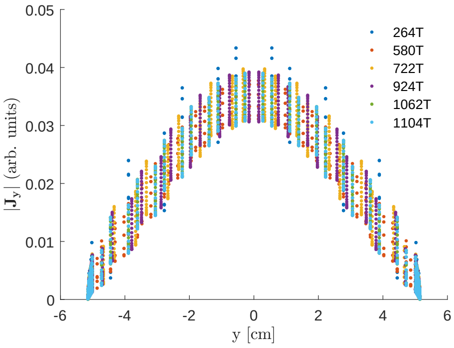

(a) $D = 3$ mm

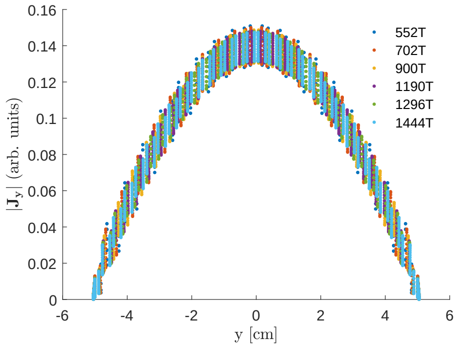

(b) $D = 1$ mm

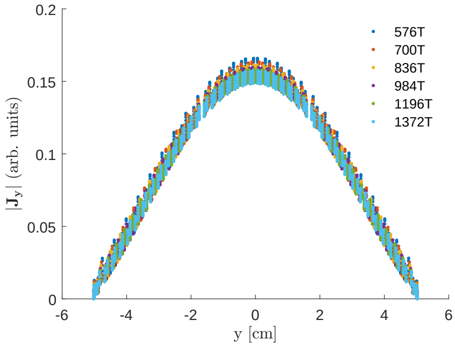

(a) $D = 0.5$ mm

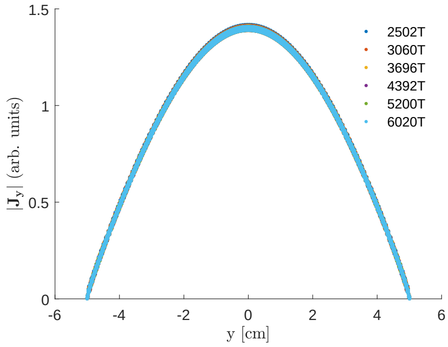

(b) $D = 0.1$ mm

Figure D.1 – Surface currents on half-wave dipoles induced by plane wave. The variation in current around a cross section decreases for smaller diameters.

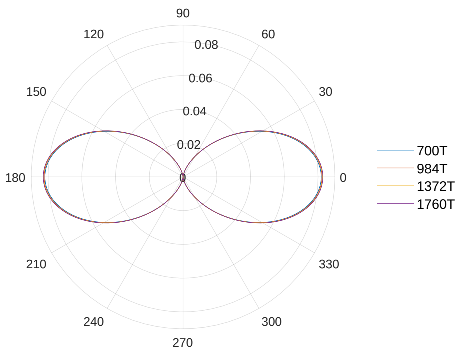

(a) $\frac{1}{2}\lambda$ dipole

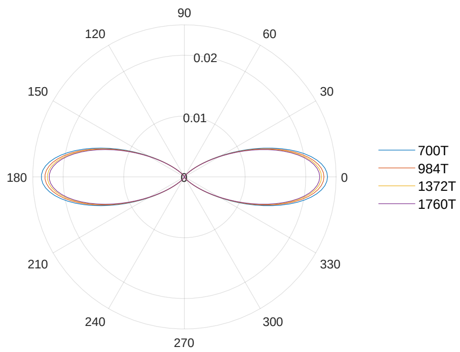

(b) λ dipole

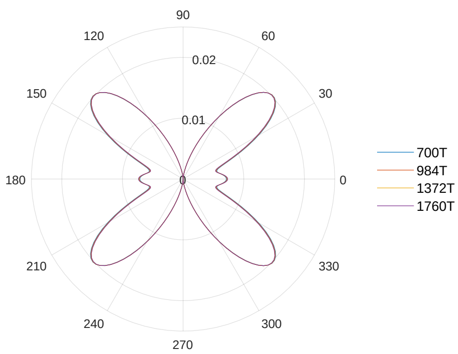

(c) $\frac{3}{2}\lambda$ dipole

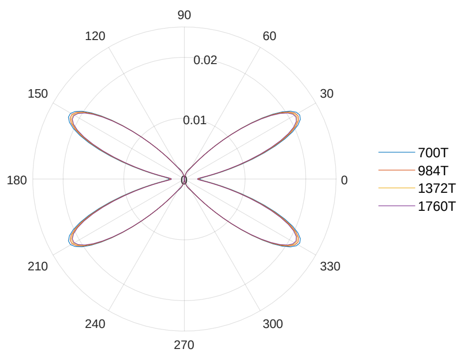

(d) 2λ dipole

FIGURE D.2 – Examination of far-field radiation pattern for $\frac{1}{2}\lambda$, λ, $\frac{3}{2}\lambda$ and 2λ dipoles.

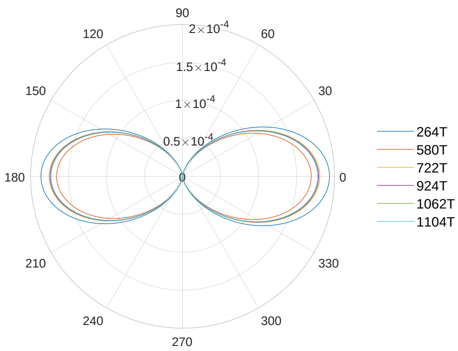

(a) $D = 3$ mm

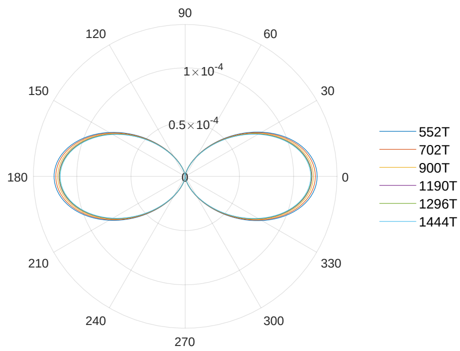

(b) $D = 1$ mm

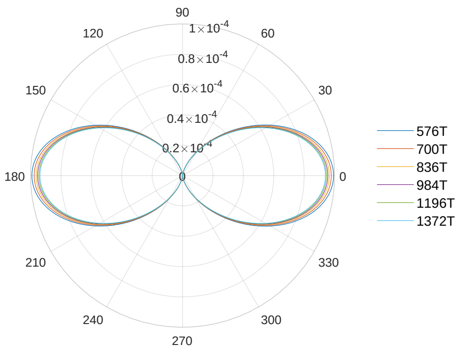

(c) $D = 0.5$ mm

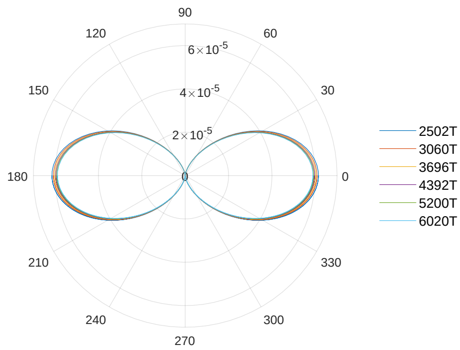

(d) $D = 0.1$ mm

FIGURE D.3 – Polar plots of the far field radiation for single dipoles diameters of $3, 1, 0.5$ and 0.1 mm in a distance of 10m. The angles vary in the zy-plane.

References

[1] W. C. Gibson. *The Method of Moments in Electromagnetics*. CRC Press, second edition, 2015. ISBN 978-1-4822-3579-1.

[2] K. R. Jha and G. Singh. *Terahertz Planar Antennas for Next Generation Communication*. Springer, 2014. ISBN 978-3-319-02341-0.

[3] TeraView, Accessed: 2018-29-08. URL `http://www.teraview.com/`.

[4] X.-C. Zhang and Jingzhou Xu. *Introduction to THz Wave Photonics*. Springer, 2010. ISBN 978-1-4419-0978-7.

[5] L. Novotny and B. Hecht. *Principles of Nano-Optics*. Cambridge University Press, second edition, 2012. ISBN 978-1-107-00546-4.

[6] D. J. Griffiths. *Introduction to Electrodynamics*. Pearson, fourth edition, 2014. ISBN 978-1-292-02142-3.

[7] D. H. Robey and D. H. Potts. Derivation of the free-space scalar green's function. *The Journal of the Acoustical Society of America*, 28(4):723–724, 1956.

[8] M. S. Tong W. C. Chew and B. Hu. *Integral Equation Methods for Electromagnetic and Elastic Waves*. Morgan & Claypool, first edition, 2009. ISBN 978-1-5982-9149-0.

[9] T. Søndergaard. *Greens Function Integral Equation Methods in Nano-Optics*. CRC Press, To be published in 2018.

[10] H. Weyl. Ausbreitung elektromagnetischer wellen über einem ebenen leiter. *Annalen der Physik*, 365(21):481–500, 1919.

[11] C. A. Balanis. *Advanced Engineering Electromagnetics*. Wiley, second edition, 2012. ISBN 978-0-470-58948-9.

[12] Roger F. Harrington. *Field Computation by Moment Methods*. Wiley-IEEE Press, 1993. ISBN 0780310144.

[13] C. A. Balanis. *Antenna Theory: Analysis and Design*. Wiley, fourth edition, 2016. ISBN 978-1-118-64206-1.

[14] D. Wilton S. Rao and A. Glisson. Electromagnetic scattering by surfaces of arbitrary shape. *IEEE Transactions on Antennas and Propagation*, 30(3): 409–418, May 1982.

[15] L. C. Godara. *Handbook of Antennas in Wireless Communications*. CRC Press, 2002. ISBN 978-0-8493-0124-7.

[16] T. F. Eibert and V. Hansen. On the calculation of potential integrals for linear source distributions on triangular domains. *IEEE Transactions on Antennas and Propagation*, 43(12):1499–1502, 1995.

[17] D. Sievers, T. F. Eibert, and V. Hansen. Correction to #8220;on the calculation of potential integrals for linear source distributions on triangular domains #8221;. *IEEE Transactions on Antennas and Propagation*, 53(9): 3113–3113, 2005.

[18] S. N. Makarov. *Antenna and EM Modeling with MATLAB*. Wiley, first edition, 2002. ISBN 0-471-21876-6.

[19] Stl file reader version 1.2. `https://se.mathworks.com/matlabcentral/\fileexchange/22409-stl-file-reader?focused=5193625&tab=function`, 2011. Accessed: 2018-21-03.